energies

MDPI

Article

Overall Efficiency Improvement of a Dual Active Bridge Converter Based on Triple Phase-Shift Control

Garry Jean-Pierre [1], Necmi Altin [2], Ahmad El Shafei [1] and Adel Nasiri [3,*]

[1] Center for Sustainable Electrical Energy Systems, University of Wisconsin-Milwaukee (UWM), Milwaukee, WI 53211, USA
[2] Electrical-Electronics Engineering Department, Faculty of Technology, Gazi University, Ankara 06560, Turkey
[3] Electrical Engineering Department, College of Engineering and Computing, University of South Carolina (USC), Columbia, SC 29208, USA
* Correspondence: nasiri@sc.edu

Abstract: This paper proposes a control scheme based on an optimal triple phase-shift (TPS) control for dual active bridge (DAB) DC–DC converters to achieve maximum efficiency. This is performed by analyzing, quantifying, and minimizing the total power losses, including the high-frequency transformer (HFT) and primary and secondary power modules of the DAB converter. To analyze the converter, three operating zones were defined according to low, medium, and rated power. To obtain the optimal TPS variables, two optimization techniques were utilized. In local optimization (LO), the offline particle swarm optimization (PSO) method was used, resulting in numerical optimums. This method was used for the low and medium power regions. The Lagrange multiplier (LM) was used for global optimization (GO), resulting in closed-form expressions for rated power. Detailed analyses and experimental results are given to verify the effectiveness of the proposed method. Additionally, obtained results are compared with the traditional single phase-shift (SPS) method, the optimized dual phase-shift (DPS) method, and TPS method with RMS current minimization to better highlight the performance of the proposed approach.

Keywords: DAB; Lagrange multiplier; power loss optimization; PSO; TPS

check for updates

Citation: Jean-Pierre, G.; Altin, N.; El Shafei, A.; Nasiri, A. Overall Efficiency Improvement of a Dual Active Bridge Converter Based on Triple Phase-Shift Control. *Energies* **2022**, *15*, 6933. https://doi.org/10.3390/en15196933

Academic Editors: Tibor Vince and Dobroslav Kovac

Received: 4 August 2022
Accepted: 13 September 2022
Published: 22 September 2022

Publisher's Note: MDPI stays neutral with regard to jurisdictional claims in published maps and institutional affiliations.

Copyright: © 2022 by the authors. Licensee MDPI, Basel, Switzerland. This article is an open access article distributed under the terms and conditions of the Creative Commons Attribution (CC BY) license (https://creativecommons.org/licenses/by/4.0/).

1. Introduction

The DAB converter is capable of providing bidirectional power flow, operating under wide voltage gain ratios, and achieving zero-voltage switching (ZVS). It has been extensively utilized in various applications, such as energy storage systems, microgrids, solid-state transformers, on-board electrical vehicle chargers, and power electronic traction transformers [1]. Although the DAB converter has many positive characteristics, some limitations exist. When utilizing the conventional singe phase-shift (SPS) modulation technique, the performance of the DAB converter depends on the operating power range. At a low power operation, conventional SPS results in a high-circulating current, which degrades the performance significantly. This circulating current does not assist in the power transfer of the converter, but serves as a heat source, resulting in conduction and copper losses, which lead to decreased efficiency of the converter. The loss of ZVS also impacts the switching losses of the DAB converter [2].

Efficiency optimization is a research focus when it comes to enhancing the DAB converter performance. Achieving high efficiency while operating at non-rated conditions or low power levels can be cumbersome. Therefore, some trade-offs are made when designing DAB converters. Some researchers have addressed the need for efficiency improvement by reconfiguring the DAB converter. Such techniques include increasing the tap of the transformer, using variable inductors, and adding or rearranging the switches [3–5]. Since these techniques need additional components and increase the system complexity, the

modification of the conventional modulation method employed to regulate the converter voltage and/or current has been studied [6,7].

Regarding control modifications, various modulation techniques have been studied to maximize the DAB converter performance. These techniques can be classified based on their control degree of freedom. The simplest and most commonly used modulation method is SPS modulation. This modulation technique regulates the power flow using only one control degree of freedom [8–10]. The switch pairs (on both the primary and secondary bridges) are gated to achieve phase-shifted square waves while maintaining a fixed 50% duty ratio. The amount and direction of the power transferred are dictated by the phase-shift control among the primary and secondary bridges [11]. It is well documented that the traditional SPS method is optimal at unity voltage ratio and rated power. However, when the system operates away from the unity voltage ratio and rated power, the SPS method has significant drawbacks, including low efficiency and high RMS and peak currents.

To address the shortcomings of SPS, multiple modulation strategies have been proposed. The extended phase-shift (EPS) [12] and dual phase-shift (DPS) [13] modulation methods have been studied to improve the control flexibility of the DAB. Both techniques contain two control variables: the power angle and the duty ratio. In the EPS method, one duty ratio is utilized to create a phase shift between the switch pairs in one full bridge. This results in the AC output voltage of that bridge being a three-level waveform while the other is a two-level 50% square wave [12]. In the DPS method, both the primary and secondary bridges utilize an equal duty ratio. In both methods, the duty ratios are used in addition to the power angle among the primary and secondary voltages.

Ref. [14] proposed a hybrid EPS modulation plus direct power control to improve the efficiency and dynamic performance of the DAB converter, while [15] proposed a linearized modulation technique based on the EPS method to minimize the conduction loss of the DAB. In [16], a broader optimization approach based on both EPS and DPS was proposed to improve the performance and efficiency of DAB converters. In [17], a PWM method was introduced to generate a three-level PWM voltage to drive each full-bridge to improve the RMS and peak currents and total efficiency. The EPS control technique was studied in [12] to enable the DAB converter to operate under soft-switching, and in [18] to minimize the reactive power loss and naturally obtain ZVS. The DPS method was presented in [19] to increase the efficiency of the DAB converter. While the EPS and DPS methods can significantly improve the DAB performance, it is worth noting that they do not provide a global optimization solution for efficiency improvement.

The TPS modulation technique [20] regulates the power angle and the duty ratios of the two full bridges independently. SPS, EPS, and DPS controls are all subcategories of TPS. The same power flow can be achieved with different phase angles and duty cycle values, which provide the required freedom to determine the optimal values. This technique has been widely used to obtain a more general solution for improving the performance of the DAB converter at different power ratings. In [21–27], the TPS method was used to achieve minimum current stress. In [28], it was used to obtain the minimum reactive power flow within the DAB converter, and in [29,30], for minimizing the RMS current of the inductor.

Other researchers have studied more advanced TPS-based modulation techniques. Ref. [31] proposed a TPS-based nondominated sorting genetic algorithm 2 for an AC–DC and DAB converter to minimize the conduction, dead band, and switching losses of the converter. Ref. [32], with a goal of reducing the conduction and switching losses, proposed a TPS-based piecewise analytical approach to derive the final hybrid closed-loop control. Ref. [33] presented a multi-objective efficiency optimization approach to extend the power range of the DAB converter using a TPS-based genetic algorithm to obtain closed-form expressions for the control variables. Ref. [34] proposed a TPS-based perturb-and-observe tracking method to improve light load efficiency by considering only the input and output voltages, the transformer turn ratio, and the leakage inductance.

Due to the supplementary control degree of freedom of the TPS control, the formulation of the analytical expression for the optimal modulation variable is cumbersome.

To formulate a closed-form expression, the LM method was used in [21] to calculate the optimal control variables for minimum peak current stress. Ref. [22] used the Karush–Kuhn–Tucker algorithm to formulate the closed-form solutions for the global optimal control variables. The global optimal condition was presented in [35] to obtain the global solution for the minimum RMS current. A randomized optimization algorithm was introduced in [36] for obtaining the minimum current stress.

Artificial intelligence has also been applied to obtain the optimal TPS control variables. Reinforcement learning was introduced in [37] and deep deterministic policy gradient in [38] for formulating the efficiency optimization and minimum reactive power, respectively. PSO is another method that has been widely used for numerical analysis. In this work, it was used, along with the LM method, to obtain numerical values for the TPS method.

Although the TPS-based RMS current minimization method can provide some improvement in the efficiency of the system by minimizing conduction and winding losses, the improvement is sub-optimal as the method offers little effect on the switching and core losses. Contrary to the RMS current minimization method, which only affects two sources of loss, and the peak current minimization method, which affects only the switching loss, this paper proposes the overall power loss of the converter as the objective function to be minimized. The power loss minimization (PLM) method affects all four major sources of loss in the system: the switching, conduction, core, and winding losses. This results in greater improvement in the efficiency of the system. Detailed formulations of each of the four sources of loss for three operation zones are obtained and analyzed using the TPS method. These equations are used to formulate the final total loss expressions for each operation zone. The resulting loss expressions are then minimized to find the optimal TPS control variables based on two optimization methods, PSO and LM. In LO, the offline PSO method is used, resulting in a numerical value. In GO, the LM is used, resulting in a closed-form expression. In the case of LO, although the optimal duty ratios that minimize the total power loss are not necessarily the optimal values for the minimum RMS current or peak current stress, they still provide the best overall efficiency due to their inclusion of all four sources of power loss. Conversely, in the case of GO, optimal duty ratios minimize the RMS current, peak current, and power loss simultaneously for the entire power range, while providing the highest efficiency. The proposed method is validated with simulation and experimental studies.

2. DAB Converter Analysis

Figure 1 shows the DAB converter setup. The switching patterns, primary and secondary voltages, and leakage inductor current under TPS conditions for the DAB converter are presented in Figure 2. When the TPS control modulation scheme is used to regulate the DAB converter, the analyses can be divided into six regions, as presented in [39]. Three regions are retained and defined with their respective boundary conditions to calculate the total power loss of the converter. In the low power region (Zone-1), the power flow has the following constraint: $0 \leq D_2 \leq \phi \leq D_1 \leq 1$. The medium power region (Zone-2) is defined by $0 \leq D_2 \leq D_1 \leq \phi \leq 1$. The high power region (Zone-3) has $0 \leq D_1 \leq D_2 \leq \phi \leq 1$ as the boundary condition. Derivation of the boundary conditions can be found in [39]. Figures 3–5 depict Zones-3, -2, and -1, respectively. The duty cycle ratio of the first full-bridge is D_1 and the second full bridge is D_2. ϕ is the phase-angle between V_1 (primary side converter output voltage) and V_2 (secondary side converter output voltage). To minimize the total power loss, the efficiency of the DAB converter is formulated in terms of the semiconductor losses (conduction and switching) and HFT losses (winding and core), depending on the manipulated variables D_1, D_2, and ϕ. Analyses of each component of the total loss are presented for each of the three zones.

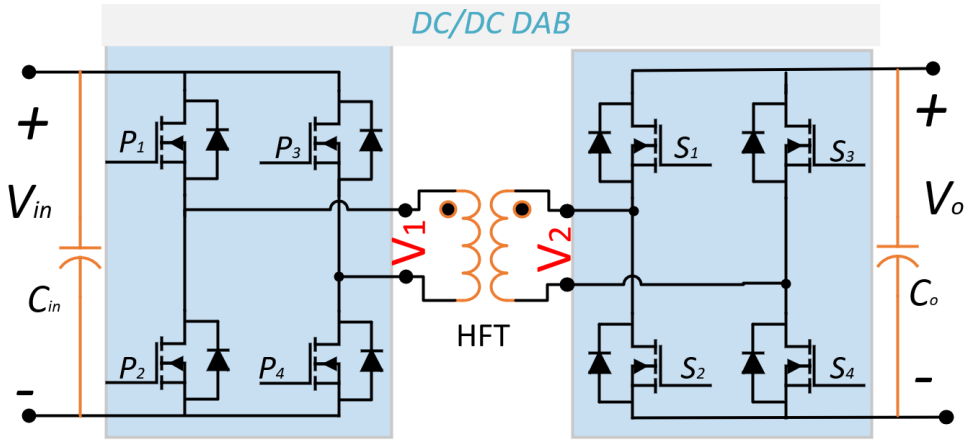


Figure 1. DAB converter.

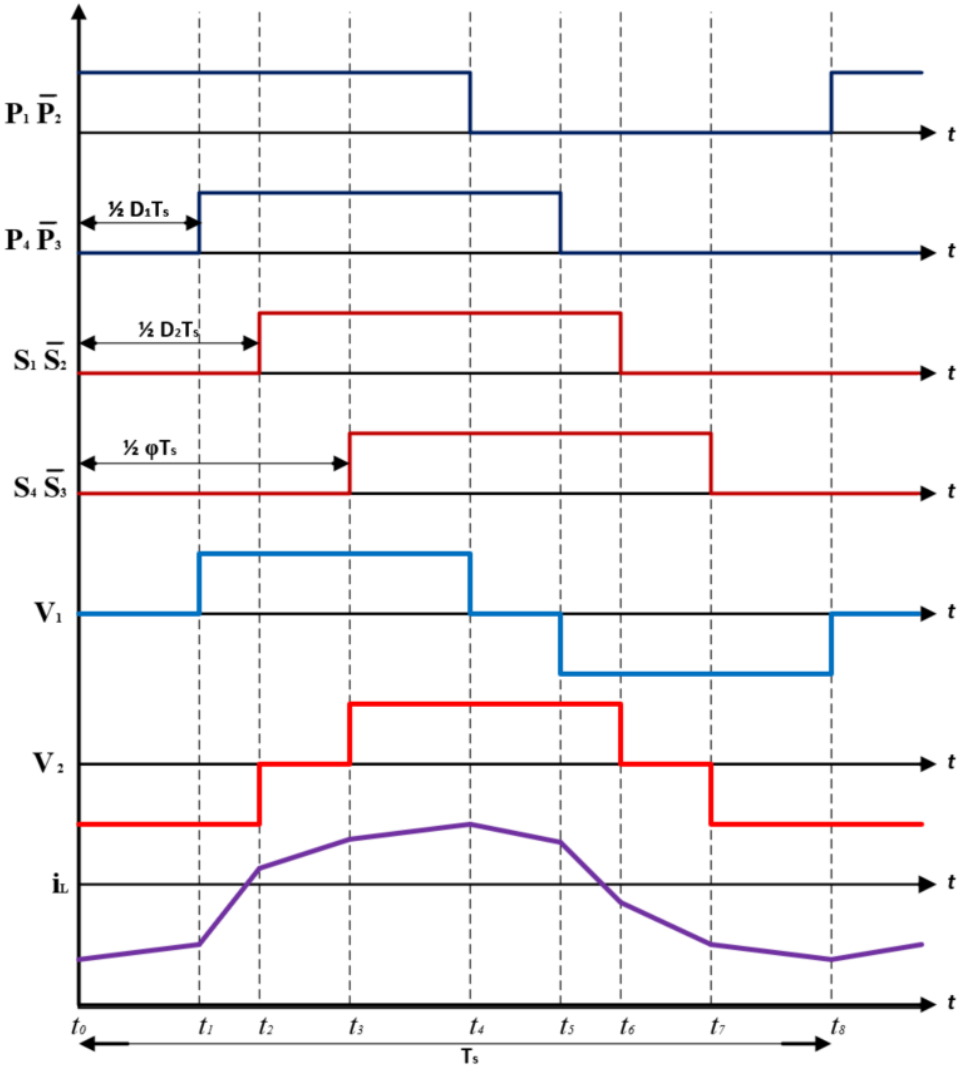


Figure 2. Gate signals, primary and secondary voltages, and current under the TPS modulation method.

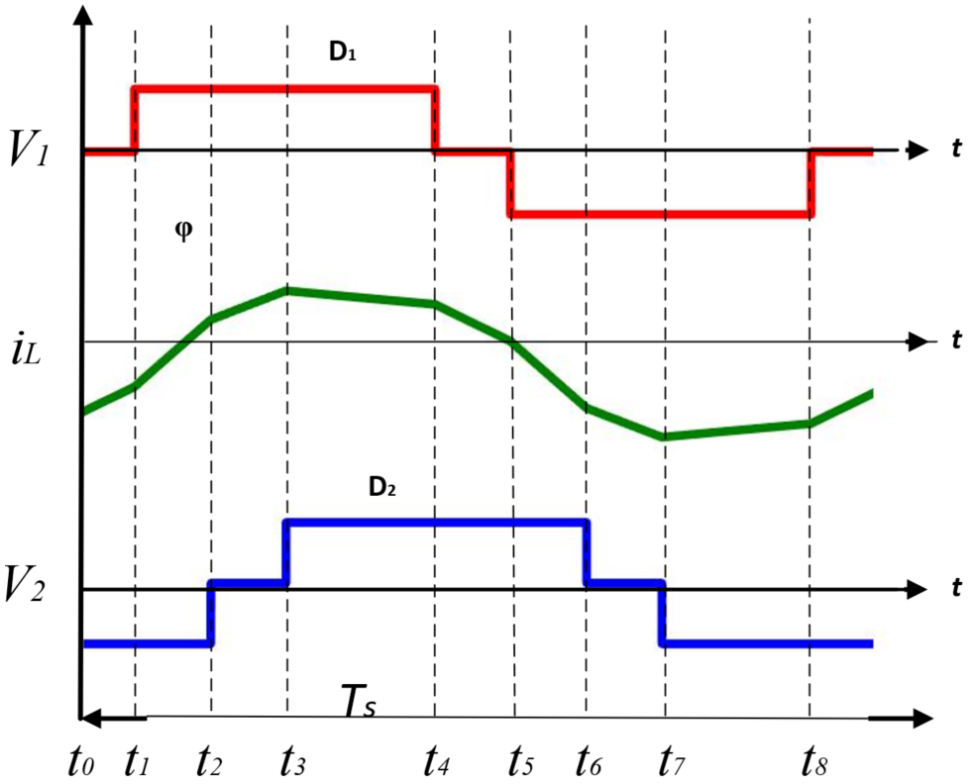


Figure 3. Primary and secondary voltages, and current under the TPS modulation method for Zone-3.

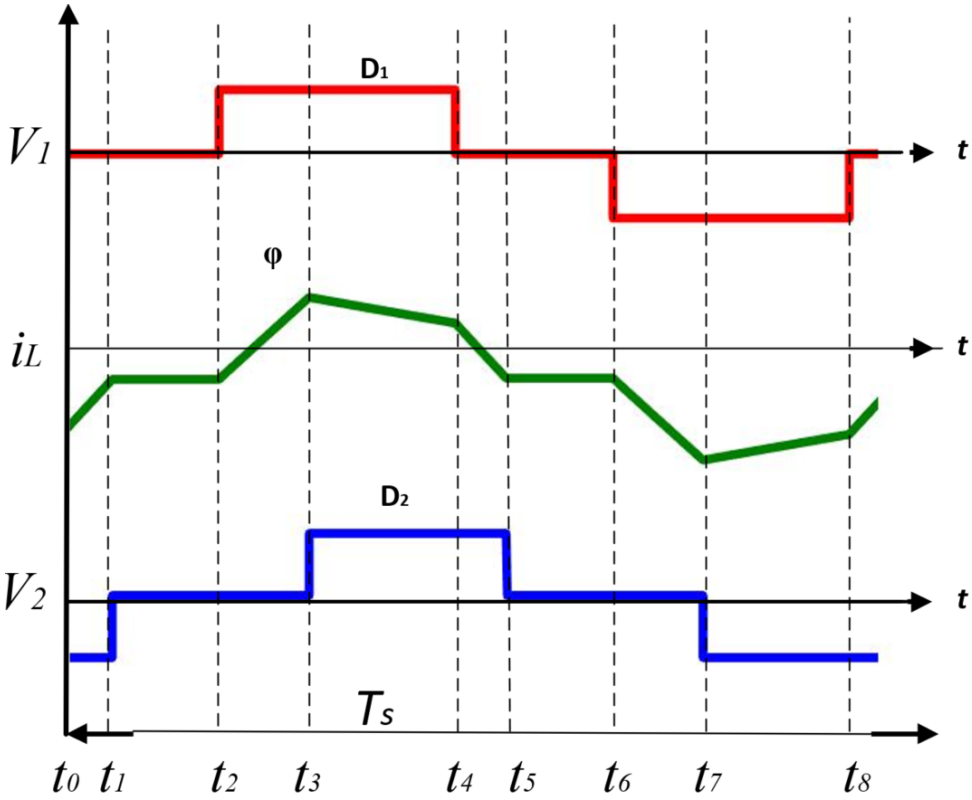


Figure 4. Primary and secondary voltages, and current under the TPS modulation method for Zone-2.

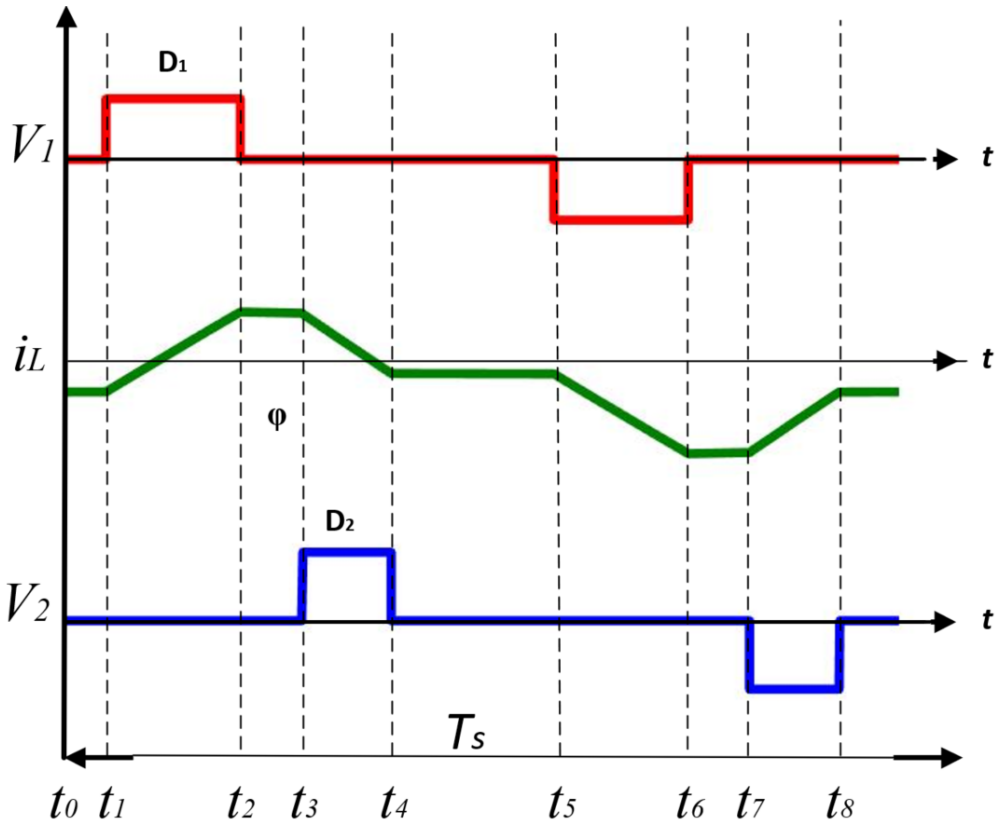


Figure 5. Primary and secondary voltages, and current under the TPS modulation method for Zone-1.

2.1. RMS Current and Average Power Formulation

To obtain the RMS current and average power, the expressions for the instantaneous values are formulated. For the theoretical analysis of both RMS current and PLM, the following assumptions are made to derive the TPS modulation scheme of a DAB module:

- The magnetizing inductance L_m is about 100 times larger than the leakage inductance L_l; therefore, the magnetizing current can be neglected.
- The turn ratio of the transformer guarantees that the module is always operated in boost mode.
- The switching cycle is about 100 times bigger than the commutation intervals; the commutation intervals are negligibly small in comparison to the switching cycle.

The instantaneous current $(i(t))$ is calculated for each region of operation based on (1)

$$(i(t)) = I_0 + \frac{1}{L}\int_{Z_a}^{Z_B}(v_1(t) - v_2(t))\,dt \tag{1}$$

where I_0 is the initial current value. In (1), Z_A and Z_B can be $t_0 - t_8$. The output current may not be vertically symmetrical. After the transient, however, the current is symmetric around the t axis. As a result, the average of the current must be calculated and subtracted from the instantaneous current. The average current is obtained, as in (2).

$$I_{ave} = \frac{1}{8}\sum_{i=1}^{8}\int_{Z_a}^{Z_B}(i(t))\,dt \tag{2}$$

The average power (P_{ave}) is calculated piecewise in each region from (3), where V_1 and I are variables, depending on the operating zone. The RMS current is formulated, as in (4).

$$P_{ave} = \frac{1}{8} \sum_{i=1}^{8} v_1(t) \int_{Z_{ai}}^{Z_{Bi}} ((i(t)) - I_{ave})\, dt \tag{3}$$

$$I_{rms} = \sqrt{\frac{1}{8} \sum_{i=1}^{8} \int_{Z_{ai}}^{Z_{Bi}} ((i(t)) - I_{ave})^2\, dt} \tag{4}$$

2.2. Semiconductor Power Losses

Conduction and switching losses are the two semiconductor losses considered for this analysis. Based on the current and voltage waveforms for each interval, as seen in Figure 2, conduction losses are developed for each semiconductor device, diode, and transistor. The on-state transistor voltage is V_{on}. V_d is the diode forward voltage drop. The current during the conduction intervals is $I_{Lt_x \to t_y}$. Based on Figure 2, switching losses are computed for each switching event. The voltages at turn-on and turn-off are V_x and V_y, respectively. I_{Lp_i} is the peak current during each switching event, t_f is the fall time, and C_{dev} is the snubber capacitor of the transistor. Owing to the ability of the converter to operate in either hard-switching or soft-switching, the ZVS constraint is established when the I_l zero crossing is within the time interval where V_1 and V_2 have opposite polarities. When operating under soft-switching, only turn-off losses are calculated. While working under hard-switching, turn-on losses are also considered. The governing equations for the conduction and switching losses are formulated, as in (5) and (6).

$$\begin{aligned} P_{cond} = {} & \frac{1}{T_s} \int_{t_x}^{t_y} |I_{L_{(tx \to ty)}}| V_{on}\, dt \\ & + \frac{1}{T_s} \int_{t_x}^{t_y} |I_{L_{(tx \to ty)}}| V_d\, dt \end{aligned} \tag{5}$$

$$P_{sw} = \frac{1}{2} V_x I_{Lpi} t_f f_s + \frac{1}{2} C_{dev} V_y^2 f_s \tag{6}$$

where f_s and T_s are the switching frequency and period, respectively.

To formulate the DAB converter power losses for high power operation in Zone-3, as depicted in Figure 3, the currents at each switching event and interval during conduction are formulated, as in (7) and (8), respectively.

$$\begin{aligned} I_{Lp1} &= \frac{V_1(1 - D_1) + V_2(\phi + D_2 - 1)}{4Lf_s} \\ I_{Lp2} &= \frac{V_1(D_1 - 1) + V_2(1 + \phi - 2D_1 + D_2)}{4Lf_s} \\ I_{Lp3} &= \frac{V_1(-1 - D_1 + 2D_2) + V_2(1 + \phi - D_2)}{4Lf_s} \\ I_{Lp4} &= \frac{V_1(-1 - D_1 + 2\phi) + V_2(1 + \phi - D_2)}{4Lf_s} \end{aligned} \tag{7}$$

$$
\begin{aligned}
I_{L(t0\to t1)} &= \frac{V_1(D_1-1)-V_2(\phi-2D_1+D_2-1)}{4Lf_s}\\
I_{L(t1\to t2)} &= \frac{V_1(D_1-2D_2-1)-V_2(\phi-D_2-1)}{4Lf_s}\\
I_{L(t2\to t3)} &= \frac{V_1(D_1-2\phi-1)-V_2(\phi-D_2-1)}{4Lf_s}\\
I_{L(t3\to t4)} &= \frac{V_1(1-D_1)-V_2(1+\phi+D_2)}{4Lf_s}\\
I_{L(t4\to t5)} &= \frac{V_1(1-D_1)-V_2(1+\phi-2D_1+D_2)}{4Lf_s}\\
I_{L(t5\to t6)} &= \frac{V_1(1+D_1-2D_2)-V_2(1+\phi-D_2)}{4Lf_s}\\
I_{L(t6\to t7)} &= \frac{V_1(1+D_1-2\phi)-V_2(1+\phi-D_2)}{4Lf_s}\\
I_{L(t7\to t8)} &= \frac{V_1(D_1-1)-V_2(-1+\phi+D_2)}{4Lf_s}
\end{aligned}
\tag{8}
$$

Here, $I_{Lp1} = -I_{Lp}(t_0) = I_{Lp}(t_4) = -I_{Lp}(t_8)$, $I_{Lp2} = -I_{Lp}(t_1) = I_{Lp}(t_5)$, $I_{Lp3} = I_{Lp}(t_2) = -I_{Lp}(t_6)$, and $I_{Lp4} = I_{Lp}(t_3) = -I_{Lp}(t_7)$.

The final conduction and switching losses for Zone-3 are obtained by substituting (7) and (8) into (5) and (6), as given below:

$$P_{SW} = \frac{AV_1t_f + BV_2t_f}{8L} \tag{9}$$

$$
\begin{aligned}
A &= |V_1 - V_2 + \phi V_2 + D_1V_1 - 2D_2V_1 - D_2V_2|\\
B &= |V_1 - V_2 + \phi V_2 - D_1V_1 + D_2V_2|
\end{aligned}
$$

$$P_{cond} = \frac{V_fA}{2Lf_s^2} - \frac{V_fB}{2Lf_s^2} - \frac{\sqrt{2}R_{ds}K}{96Lf_s^2} + \frac{V_fD_1I}{2Lf_s^2} - \frac{V_fJ}{2Lf_s^2} \tag{10}$$

$$
\begin{aligned}
A &= |(\phi-1)(\phi V_1 - D_1V_1 + D_2V_2)|\\
B &= |((1-\phi+D_2)V_2 + (\phi - D_1 + D_2 - 1)V_1)|(D_2-\phi)\\
C &= -4D_1^3 - 6D_1D_2^2 + 6D_1^2D_2 + 6D_1^2\phi\\
E &= -6D_1^2 + 6D_1D_2 - 6D_2^2 - 6D_1\phi^2 + 6D_1\phi\\
F &= 4D_2^3 + 4\phi^3 - 6\phi^2 + 2\\
G &= 3(D_2-\phi)^2 + 2(D_2-\phi)^3 - 1\\
H &= 3D_1^2 - 1 - 2D_1^3\\
I &= |V_1(1-D_1) + (-1+\phi-D_1+D_2)V_2|\\
J &= |V_2(-\phi+D_1) + (-1+D_2)V_1|(D_1-D_2)\\
K &= V_1V_2(C+E+F) + V_2^2G + V_1^2H
\end{aligned}
$$

2.3. HFT Power Losses

The HFT total losses are the combination of the core and winding losses. To formulate the winding loss, the RMS current is determined and both the skin and proximity effect are considered for calculating R_{eff}. Due to the non-sinusoidal waveform characteristic for the given applications, the improved generalized Steimetz Equation [40] is used to obtain the closed-form expression for the core loss. The driving equations for the winding and core losses are formulated in (11) and (12), respectively.

$$P_{W_{loss}} = R_{eff}I_{rms}^2 \tag{11}$$

$$R_{eff} = \frac{MLT_w N}{\pi \sigma r_l^2 N_s}\left(1 + \frac{\pi^2 N_s \beta}{192}\left(16m^2 - 1 + \frac{24}{\pi^2}\right)\left(\frac{r_l}{\sigma}\right)^4\right)$$

$$P_{core} = \frac{1}{T_s}\int_0^{T_s} K_i \left|\frac{dB(t)}{dt}\right|^{\gamma} (\Delta B)^{\theta-\gamma}\, dt \tag{12}$$

$$K_i = \frac{2^{1-\theta} K_s \pi^{1-\gamma}}{\frac{1.7061}{\gamma+1.354} + 0.2761}$$

To obtain the final expression for the winding losses, the RMS current for each zone needs to be calculated using (4). By substituting (13) into (11), the winding loss expression is obtained, as in (14).

$$I_{rms-Z3} = \frac{\sqrt{3}}{3}\frac{\left(J + 2V_2^2\left(D - 6E + 3F - 1\right)\right)^{\frac{1}{2}}}{4Lf_s} \tag{13}$$

$$\begin{aligned}
A &= 3D_1(D_1D_2 + D_1\phi - D_1 - D_2^2 + D_2 + \phi - \phi^2)\\
B &= 3(D_2^3 - D_2^2 - \phi^2) + 2(\phi^3 - D_1^3) + 1\\
C &= 3D_1^2 - 2D_1^3 - 1\\
D &= 2(D_2^3 - \phi^3)\\
E &= D_2^2\phi + D_2\phi^2 - D_2\phi\\
F &= \phi^2 + D_2^2\\
J &= 4V_1V_2(A + B) + 2V_1^2C
\end{aligned}$$

$$P_{Wloss} = R_{eff} I_{rms-Z3}^2 \tag{14}$$

The core loss of the HFT is formulated for Zone-3 as follows:

$$P_{core-Z3} = K_i(2B_m)^{\theta-\gamma}\left(J + B(E^{\gamma} + F^{\gamma}) + C(\gamma + (D^{\gamma}))\right) \tag{15}$$

$$\begin{aligned}
A &= \frac{T_s}{2} - \frac{\phi T_s}{2} & B &= \frac{D_2 T_s}{2} - \frac{D_1 T_s}{2}\\
C &= \frac{\phi T_s}{2} - \frac{D_2 T_s}{2} & D &= \frac{4B_m f_s}{\phi}\\
E &= \frac{2B_m}{\frac{D_2 T_s}{2} + \frac{T_s}{2}} & F &= \frac{4B_m f_s}{D_2}\\
J &= A(B_m f_s)^{\gamma}(2^{\gamma} + 4^{\gamma})
\end{aligned}$$

The average power transfer expression for Zone-3 is expressed, as in (16).

$$P_{ave-Z3} = \frac{V_1V_2A - D_2^2 + D_2 - \phi^2 + \phi}{4Lf_s} \tag{16}$$

$$A = (D_1D_2 + \phi - 1)(-D_1^2)$$

The equations for the other zones can be obtained in a similar fashion. As a result, (17)–(22) can be obtained for Zone-2, and (23)–(28) for Zone-1. The derivations can be found in [41].

$$P_{SW_{Z2}} = \frac{|V_1 t_f A| + |V_2 t_f B|}{8L} \tag{17}$$

$$A = V_1(1 - D_1) + V_2(D_2 + \phi - 1)$$
$$B = V_2(1 - \phi + D_2) + V_1(D_1 - 1)$$

$$P_{cond_{Z2}} = \frac{V_f A}{2Lf_s^2} - \frac{R_{ds} J}{3Lf_s^2} - \frac{V_f D_1 G}{2Lf_s^2} - \frac{V_f H}{2Lf_s^2} + \frac{D_2 V_f I}{2Lf_s^2} \tag{18}$$

$$A = |(\phi - 1)(V_1(\phi - D_1) + D_2 V_2)|$$
$$B = -6{D_1}^2 D_2 + 6{D_1}^2\phi - 6{D_1}^2 + 6D_1{D_2}^2 + 6D_1 D_2$$
$$C = -6D_1\phi^2 + 6D_1\phi - 6{D_2}^2 + 4\phi^3 - 6\phi^2 + 2$$
$$E = 2{D_2}^3 - 6{D_2}^2\phi + 3{D_2}^2 + 6D_2\phi^2 + a$$
$$a = -6D_2\phi - 2\phi^3 + 3\phi^2 - 1$$
$$F = -1 - 2{D_1}^3 + 3{D_1}^2$$
$$G = |V_2(-\phi + D_2 + 1) + V_1(\phi - 1)|(D_1 - \phi)$$
$$H = |V_2(-\phi + D_2 + 1) + V_1(D_1 - 1)|(D_1 - D_2)$$
$$I = |V_1(1 - D_1) + V_2(\phi - 1)|$$
$$J = V_1 V_2(B + C) + V_2^2 E + V_1^2 F$$

$$I_{rms-Z_2} = \frac{\sqrt{3}}{3} \frac{\left(2V_1 V_2(A) + F\right)^{\frac{1}{2}}}{4Lf_s} \tag{19}$$

$$A = 6(D_1^2\phi - D_1^2 D_2 - D_1^2 + D_1 D_2^2 + a + 4\phi^3 + 2)$$
$$a = D_1 D_2 - D_1\phi^2 + D_1\phi - D_2^2 - \phi^2$$
$$B = 3D_1^2 - 2D_1^3 - 1$$
$$C = 2(D_2^3 - \phi^3)$$
$$D = D_2^2\phi + D_2\phi^2 - D_2\phi$$
$$E = (\phi^2 + D_2^2)$$
$$F = 2V_1^2 B + 2V_2^2(C - 6D + 3E - 1)$$

$$P_{Wloss_{Z2}} = R_{eff} I_{rms-Z2}^2 \tag{20}$$

$$P_{core-Z_2} = K_i(2B_m)^{\theta-\gamma}\left(A(B_m f_s)^{\gamma}(2^{\gamma} + 4^{\gamma}) + E\right) \tag{21}$$

$$A = \frac{T_s}{2} - \frac{\phi T_s}{2} \qquad B = \frac{\phi T_s}{2} - \frac{D_1 T_s}{2}$$
$$C = \frac{2B_m}{\frac{\phi T_s}{2} + \frac{T_s}{2}} \qquad D = \frac{4B_m f_s}{\phi} \qquad E = B(C^{\gamma} + D^{\gamma})$$

$$P_{ave-Z_2} = \frac{V_1 V_2(D_2 - \phi^2 + \phi - D_1(D_2 - \phi + 1))}{4Lf_s} \tag{22}$$

$$P_{SW-Z_1} = \frac{|V_1 t_f B| + |V_2 t_f C| + A}{8L} \tag{23}$$

$$\begin{aligned} A &= 4C_{dev} f_s L(V_1^2 + V_2^2) \\ B &= V_1(1 - D_1) + V_2(\phi + D_2 - 1) \\ C &= (V_2(1 + D_2 - \phi) + V_1(D_1 - 1)) \end{aligned}$$

$$P_{cond-Z_1} = \frac{V_f A}{2Lf_s^2} - \frac{V_f B}{2Lf_s^2} - \frac{R_{ds} K}{3Lf_s^2} - \frac{V_f |V_2| H}{2Lf_s^2} \tag{24}$$

$$\begin{aligned} A &= D_2|V_1(1 - D_1) + V_2(\phi - 1)| \\ B &= |V_2(1 + D_2 - \phi) + V_1(D_1 - 1)|(D_2 - \phi) \\ C &= 2D_1^3 - 3D_1^2 D_2 - 3D_1^2\phi - 3D_1^2 + 3D_1 D_2^2 - 3\phi^2 \\ D &= 3D_1 D_2 + 3D_1\phi^2 + 3D_1\phi - 3D_2^2 + 1 \\ E &= 2D_2^3 - 6D_2^2\phi + 3D_2^2 + 6D_2\phi^2 \\ F &= -6D_2\phi - 2\phi^3 + 3\phi^2 - 1 \\ G &= 3D_1^2 - 2D_1^3 \\ H &= (D_1 - 1)(D_2 - D_1 + \phi) \\ K &= (2V_1 V_2(C + D) + V_2^2(E + F) + V_1^2 G) \end{aligned}$$

$$I_{rms-Z_1} = \frac{\sqrt{3}}{3} \frac{\left(V_1 V_2(A) - V_1^2 B + V_2^2 C\right)^{\frac{1}{2}}}{4Lf_s} \tag{25}$$

$$\begin{aligned} A &= (4D_1^3 + 6(D_1^2 D_2 + D_1^2\phi + D_1^2 - a + \phi^2) - 2) \\ a &= D_1 D_2^2 - D_1 D_2 - D_1\phi^2 - D_1\phi + D_2^2 \\ B &= 3D_1^2 - 2D_1^3 - 1 \\ C &= 2D_2^3 - 6D_2^2\phi + 3D_2^2 + d \\ d &= 6D_2\phi^2 - 6D_2\phi - 2\phi^3 + 3\phi^2 - 1 \end{aligned}$$

$$P_{Wloss-Z_1} = R_{eff} I_{r_{ms-Z1}}^2 \tag{26}$$

$$P_{core-Z_1} = K_i(2B_m)^{\theta-\gamma}\left(\left(\frac{T_s}{2} - \frac{D_1 T_s}{2}\right)(B_m f_s)^{\gamma}(2^{\gamma} + 4^{\gamma})\right) \tag{27}$$

$$P_{ave-Z_1} = \frac{V_1 V_2(1 - D_1)(D_2 - D_1 + \phi)}{4Lf_s} \tag{28}$$

3. DAB Control Optimization and Trajectories

Minimizing the total power loss for a given average power is the goal of optimization. D_1, D_2, and ϕ are the variables. The total power loss that needs to be minimized is the objective function, f. The constraint, g, is the average power transfer. The LM and PSO are the two optimization methods that were used. In Zone-1 and Zone-2, obtaining a closed-form expression for the optimal control degree of freedom is cumbersome due to the nonlinearity of the total power loss expression. In these two zones, only one objective function can be minimized at a time, which is referred to as LO. The optimal numerical value for the degree of freedom is obtained using PSO. In Zone-3, the average power transferred and the objective function can be used to obtain the closed-form expressions

for the TPS variables using the LM method. This is referred to as GO. Contrary to the LO method used in Zone-1 and Zone-2, the GO method used in Zone-3 covers multiple target functions, such as peak current stress, RMS current, and total power loss. Table 1 summarizes the feasible optimization method for each zone.

Table 1. Optimization methods based on the power regions.

$V_1 < V_2$	Zone-1	Zone-2	Zone-3
Objective function	Power Loss	Power Loss	Power Loss
Methods	PSO	PSO	LM
Global	-	-	√
Local	√	√	-

Based on the Lagrange optimization methodology, a Lagrange function is the combination of the objective and constraint functions multiplied by the LM variable (λ), as formulated in (29).

$$\wedge(D_1, D_2, \phi, \lambda) = f(D_1, D_2, \phi) + \lambda_g(D_1, D_2, \phi) \tag{29}$$

The optimal solution can be found by using a set of equations of the gradient of the LM, as shown in (29) and (30).

$$\vee\wedge = 0 \rightarrow \qquad \frac{\partial\wedge}{\partial D_1} = 0 \qquad \frac{\partial\wedge}{\partial D_2} = 0 \qquad \frac{\partial\wedge}{\partial \phi} = 0 \tag{30}$$

$\frac{\partial\wedge}{\partial\lambda} = 0$ is a subset of $\vee\wedge = 0$. No new information is revealed from this formulation, as it is simply the constraint function, g, itself.

In Zone-3, the closed-form expression for minimizing the power loss can be obtained, and GO can be utilized to simplify the formulation. Therefore, the RMS minimization, the peak current minimization, or the total PLM can be used as the objective function. The peak current stress (i_{lp1}) from (7) is chosen as the objective function to reduce the computational burden and the corresponding average power for Zone-3 given in (16) is used. Substituting the p.u. expressions, as formulated in (31) and (32), into (29) and (30) yields the closed-form expressions for D_1 and D_2, as formulated in (33) and (34), where $K = \frac{2V_1}{V_2}$. The rated values of the power and the peak current are computed, as follows: $P_r = \frac{V_1 V_2}{8Lf_s}$ and $I_r = \frac{V_2}{8Lf_s}$

$$P_{aave-Z3pu} = 2(D_2 - D_1 + \phi - \phi^2 - D_1 D_2 + D_1\phi) \tag{31}$$

$$I_{lp_{pu}} = \frac{2V_1}{V_2}((1-D)_1) + (\phi + D_2 - 1) \tag{32}$$

$$D_{1V_2>V_1} = 2\phi + \frac{24D_2 - 24D_2^2 + 4KD}{2\sqrt{A + 2B + C - 8D_2 + 4}} - 1 \tag{33}$$

$$A = K^2(6D_2 - 6D_2^2 - 1) \qquad B = K(6D_2^2 - 6D_2 + 1)$$
$$C = 8D_2(1 - D_2)$$
$$D = (6D_2^2 - 6D_2 + 1) - 4$$

$$D_{2V_2>V_1} = 2D_1(4 + K^2 - 6K) + E + \sqrt{2KD} \tag{34}$$

$$A = K^2(-3(2D_1 - \phi)^2) - 6D_1 + 3\phi + 1$$
$$B = K(12D_1 - 6\phi - 1 + 6(2D_1 - \phi)^2)$$
$$C = 8D_1(2\phi - 2D_1 - 1) + 4\phi(1 - \phi)$$
$$D = \frac{\sqrt{A + B + C)}}{5(7K^2 - 10K + 4)}$$
$$E = \phi(6K - K^2 - 4) + (2K - 2)^2$$

Optimal Trajectory for Zone-3

For GO, the optimal D_1, D_2, and ϕ for PLM are the same for the RMS current minimization and the peak current minimization. The boundary and optimal trajectory for Zone-3 are shown in Figures 6–9. It can be seen that the optimal duty cycles for both the primary and secondary sides are between $0.7 \leq D_1, D_2 \leq 1$ (where 1 depicts 50% duty cycle). The analytical average power transfer, total power loss, and efficiency calculation based on the optimal TPS variables are shown in Figure 8. The overall loss breakdown for this region is also depicted in Figure 9.

The offline PSO technique, Figure 10, is used for obtaining the optimal control variables for Zone-1 and Zone-2. The formulation contains two principal equations, (35) and (36).

$$X_i^{k+1} = X_i^k + V_i^{k+1} \tag{35}$$

$$V_i^{k+1} = V_i^k + C_1 r_1 (P_{best_i}^k - X_i^k) + c_2 r_2 (G_{best}^k - X_i^k) \tag{36}$$

In these equations, X is the particle position (TPS variable). V is the particle velocity used to modify the particle position (X) for every iteration. P_{best} is the best remembered individual particle position. G_{best} is the best-remembered swarm position. k is the iteration index, c_1 and c_2 are positive constants, and r_1 and r_2 are two randomly generated numbers, such that $0 \leq r_1, r_2 \leq 1$ [42].

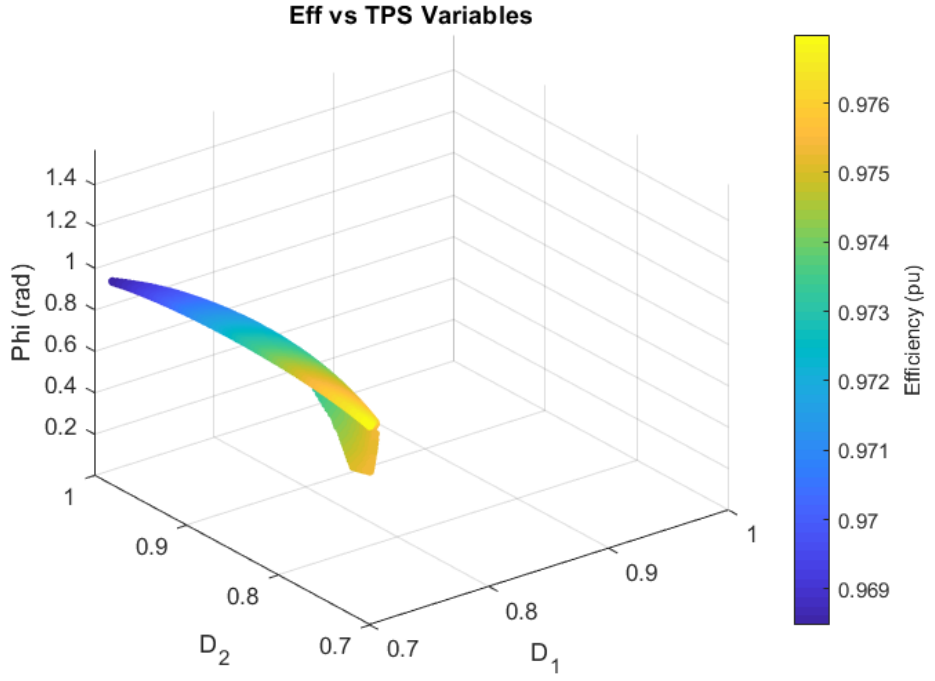


Figure 6. Optimal control variables vs. efficiency.

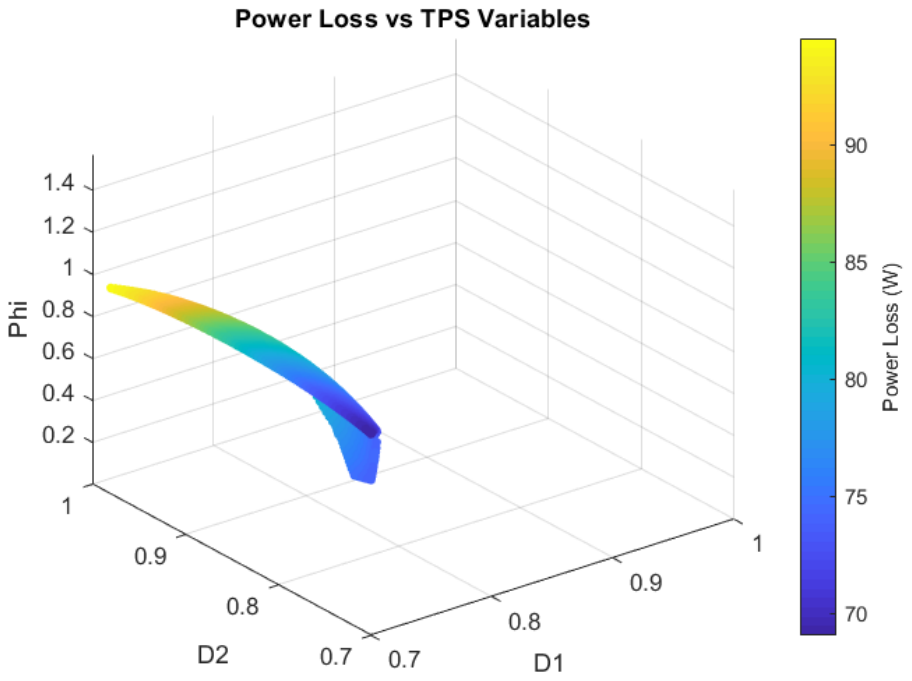


Figure 7. Optimal control variables vs. power losses.

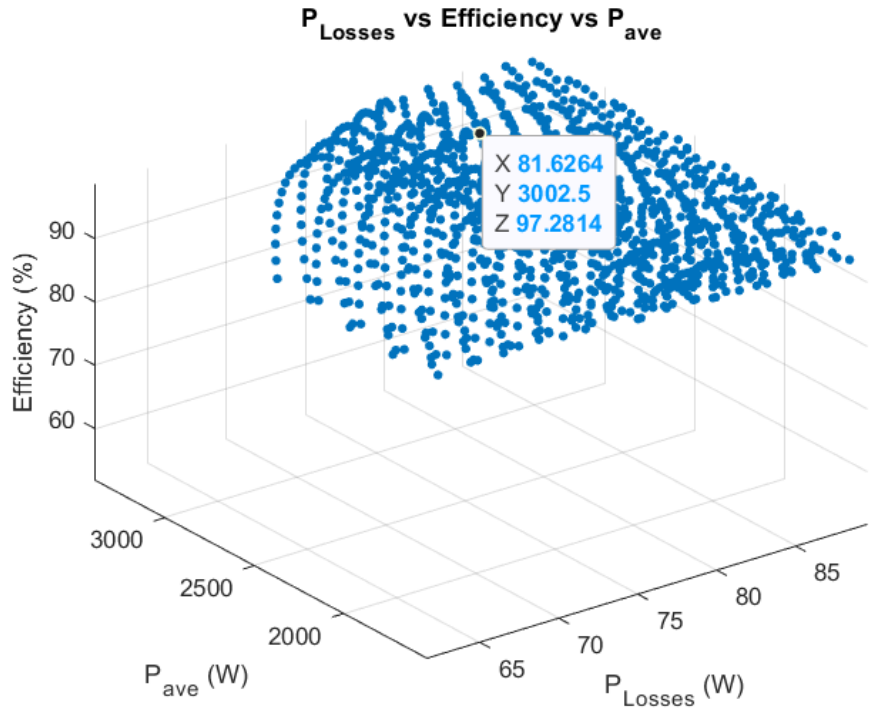


Figure 8. Analytical average power, efficiency, and power loss calculation.

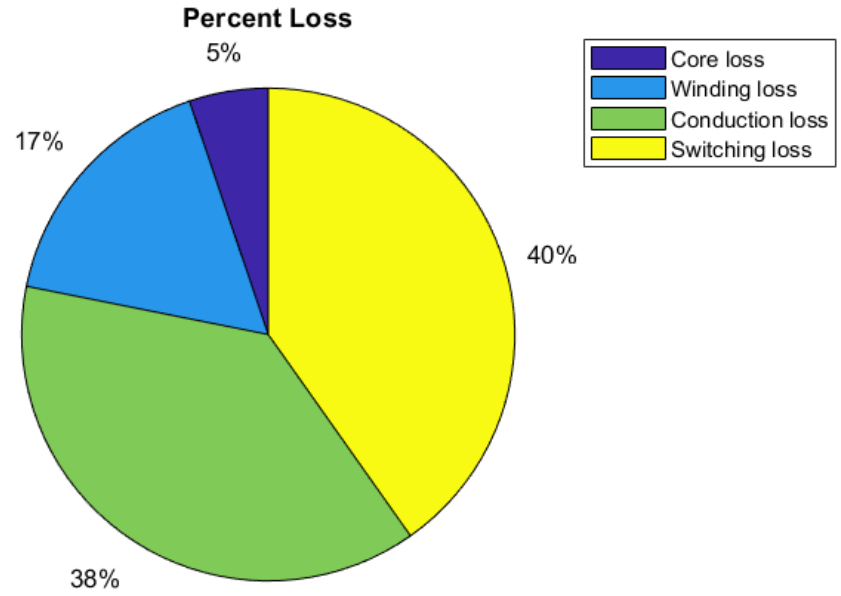


Figure 9. Loss breakdown for Zone-3.

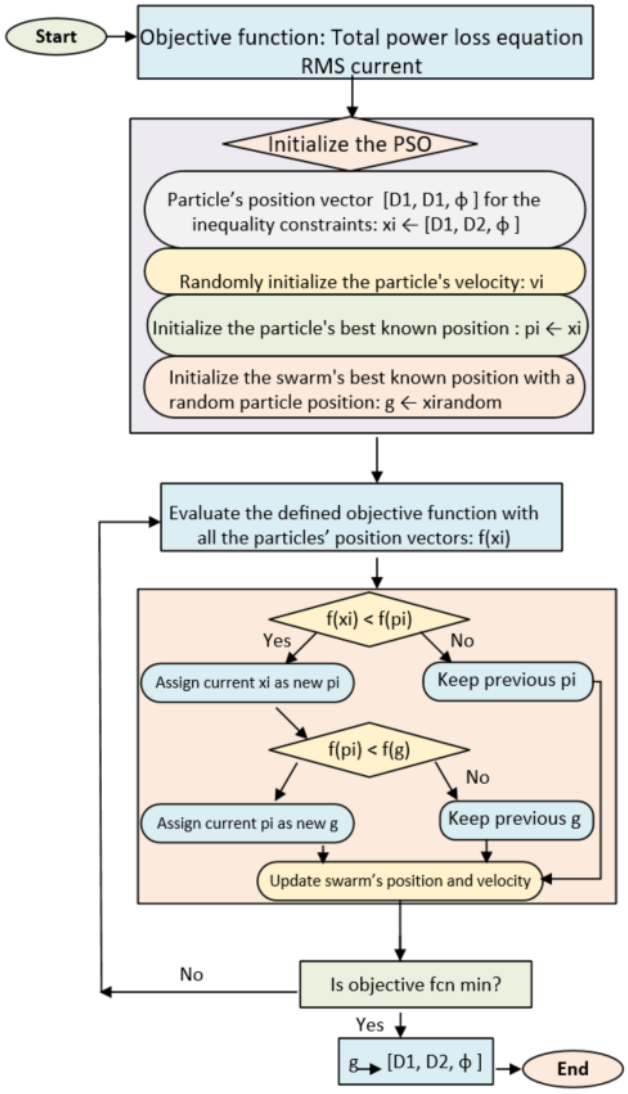


Figure 10. PSO flow chart.

4. DAB Control Structure

Figure 11 shows the optimal closed-loop control structure for the DAB converter and depicts both the buck and boost operation modes. The initial phase shift, ϕ_i, is generated by the voltage PI controller. To estimate the average power transferred from the primary to the secondary full-bridge, ϕ_i is applied in the optimal control variable generation block. The estimated average power is then used to determine the operating zone. The optimal $D_{1_o pt}$ and $D_{2_o pt}$ are calculated either from (33) and (34) for Zone-3 or are chosen from the PSO look-up table for the other operating zones.

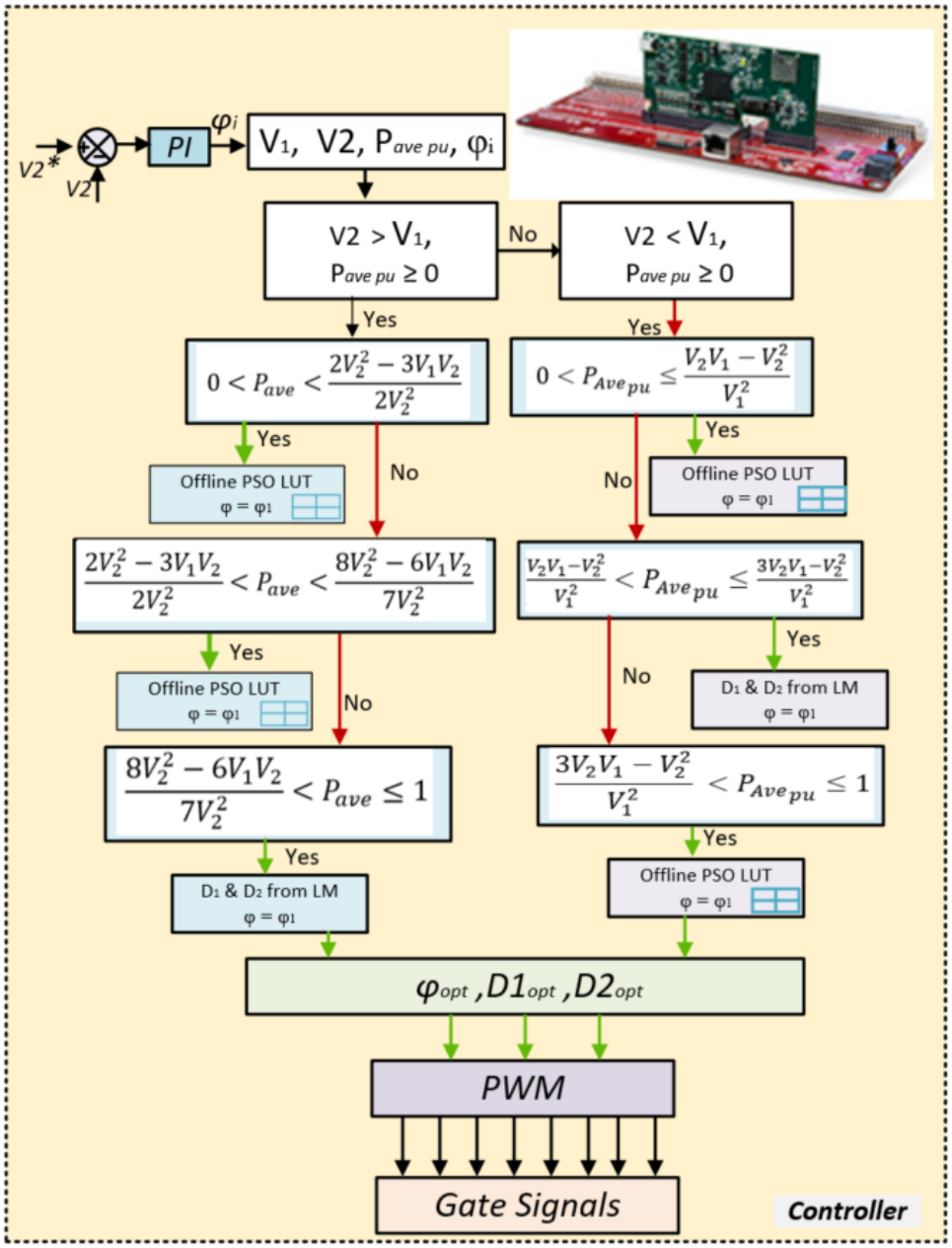


Figure 11. Optimal closed-loop control of the DAB.

5. Experimental Results

Utilizing the Typhoon HIL device and the TMDSCNCD28388D control card, as seen in Figure 11, the performance of the proposed PLM scheme for the DAB converter was tested for three cases; low power, medium power, and rated power. To validate the efficiency improvement of the proposed scheme, the TPS method with RMS current minimization

was compared to the proposed PLM method. The proposed TPS with PLM method was also compared to the traditional SPS and the optimized DPS methods. Figures 12–14 show the performances using the SPS method, Figures 15–17 show the performances for the optimized DPS control technique, and Figures 18–20 present the results for the optimized TPS with the RMS current minimization algorithm.

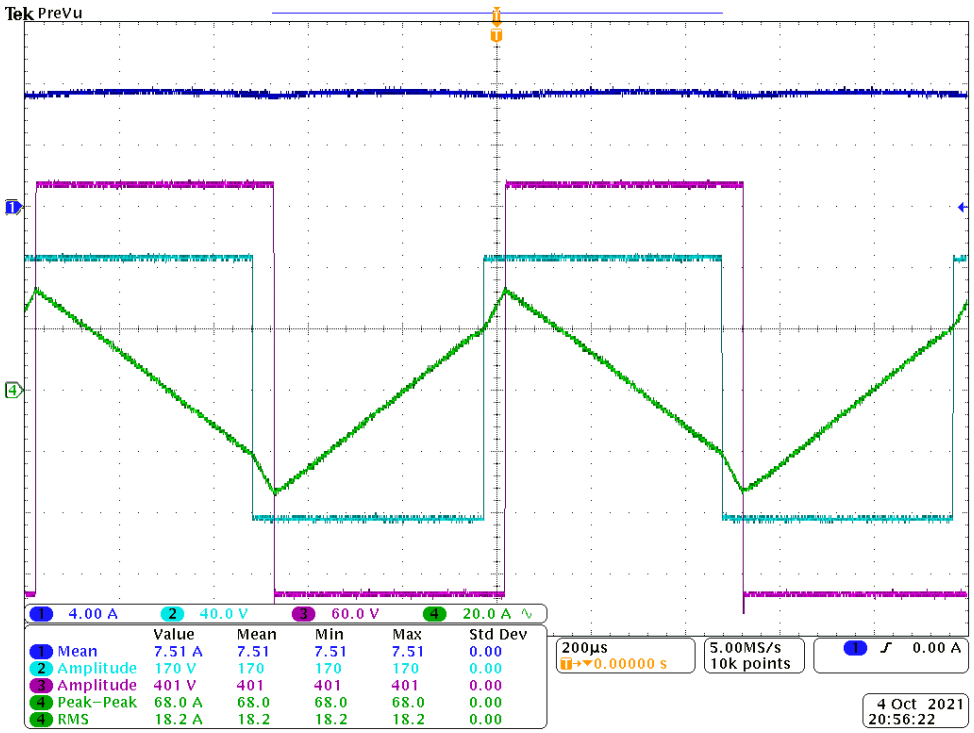


Figure 12. DAB operation at rated power under the SPS method.

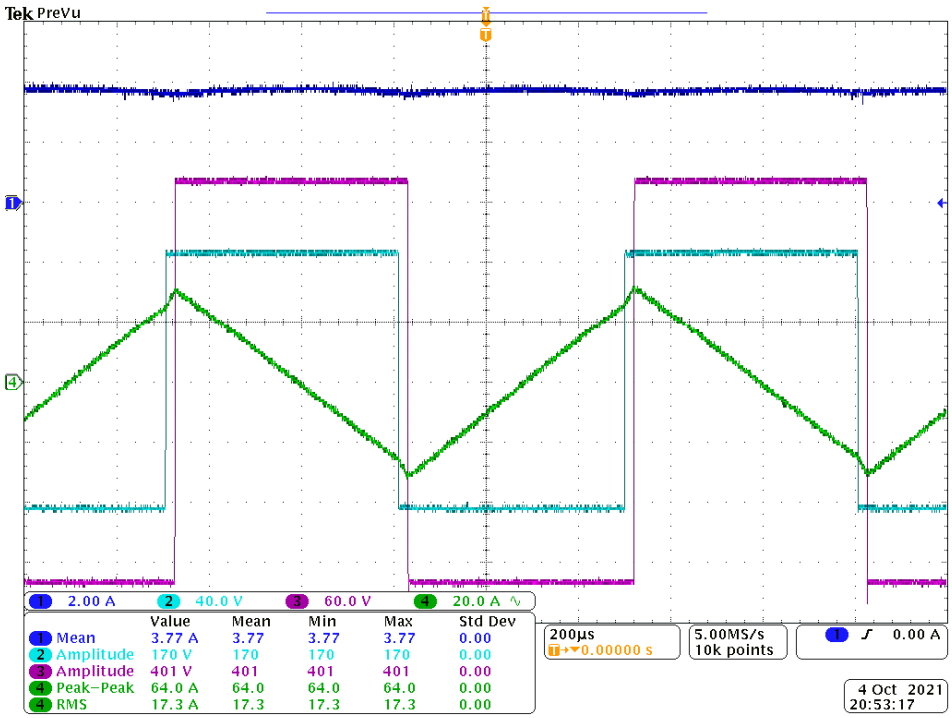


Figure 13. DAB operation at medium power under the SPS method.

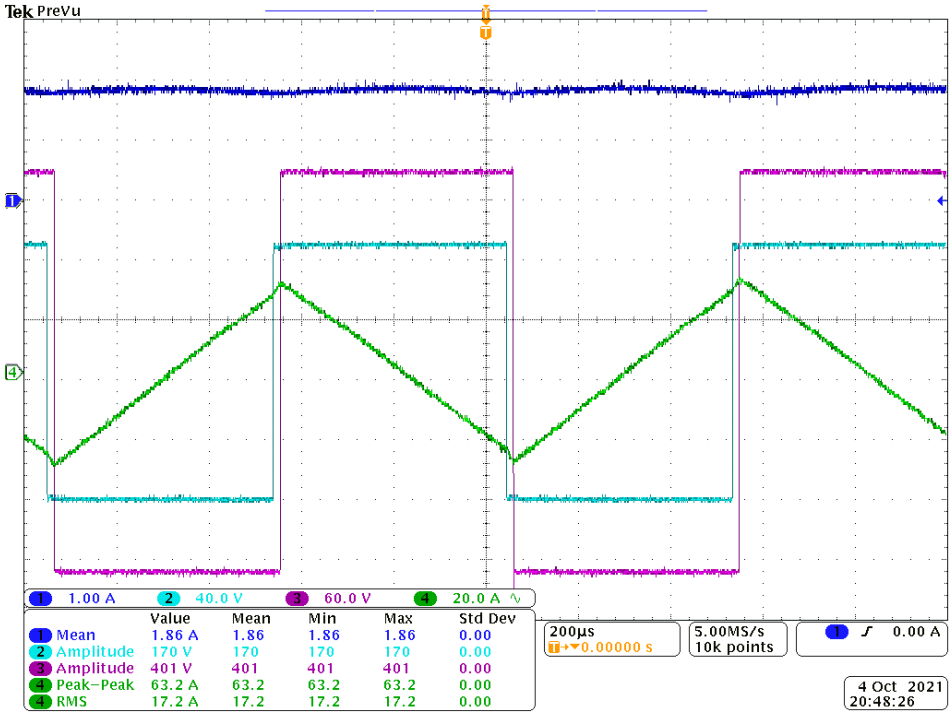


Figure 14. DAB operation at low power under the SPS method.

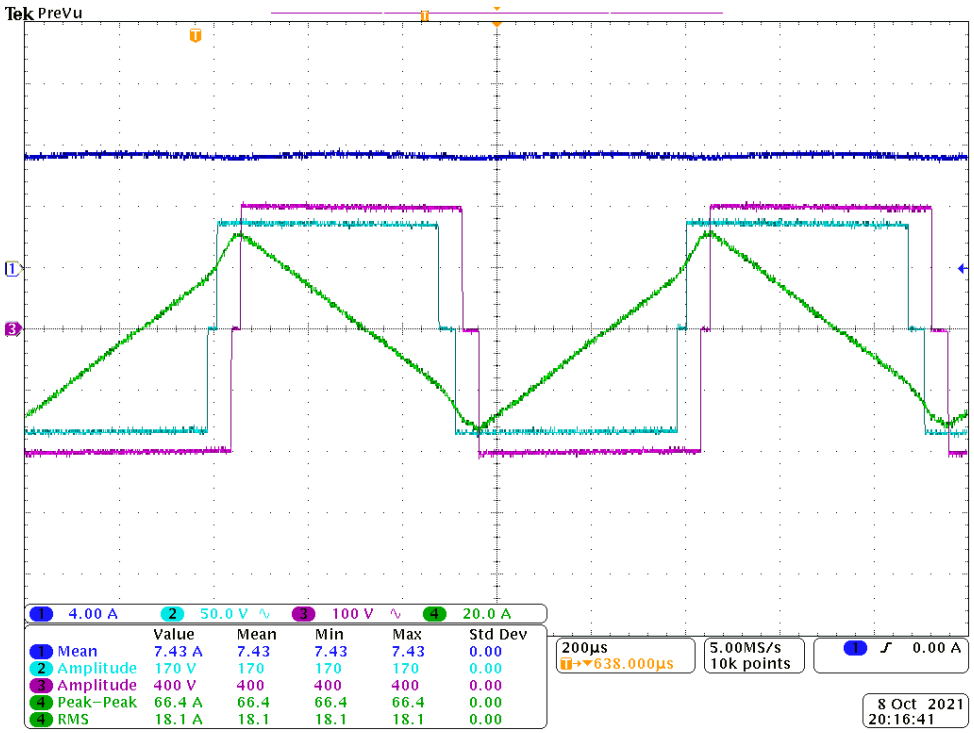


Figure 15. DAB operation at rated power under the DPS method.

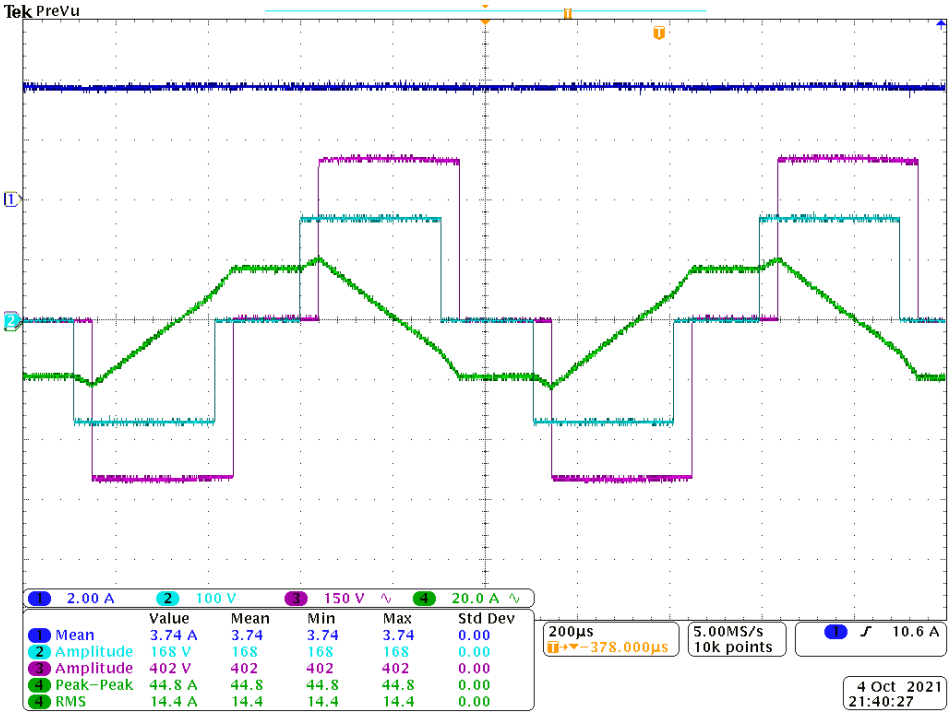


Figure 16. DAB operation at medium power under the DPS method.

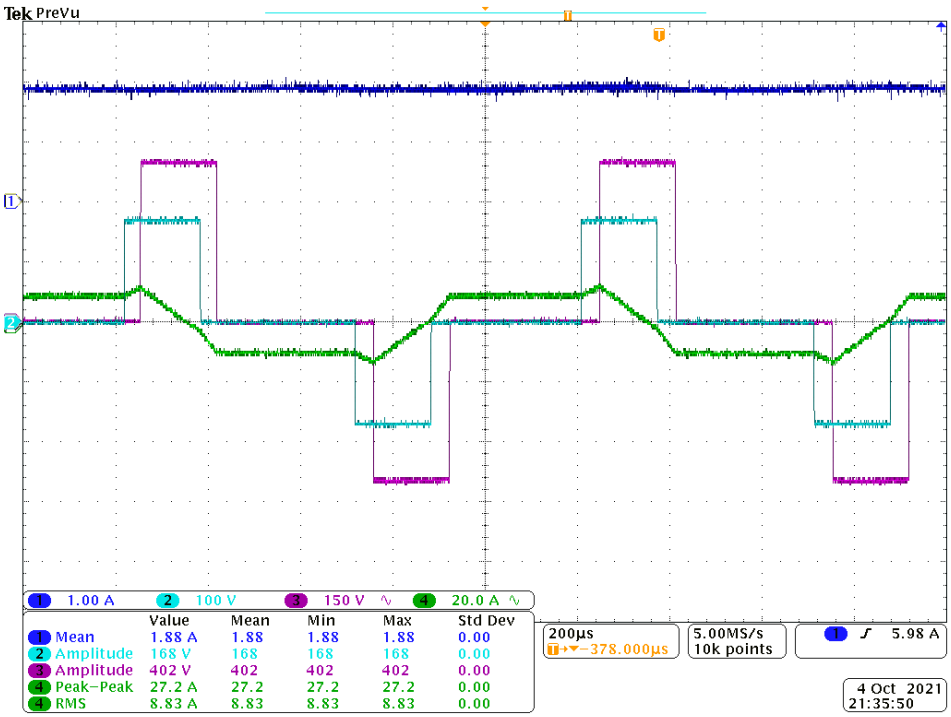


Figure 17. DAB operation at low power under the DPS method.

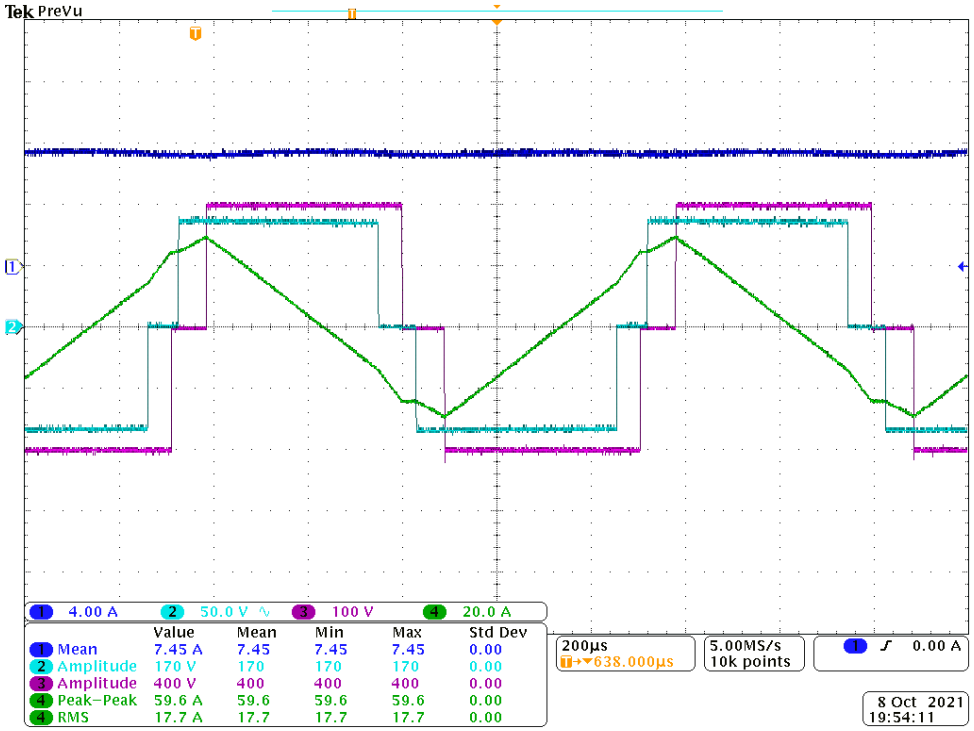


Figure 18. DAB operation under the TPS method at rated power.

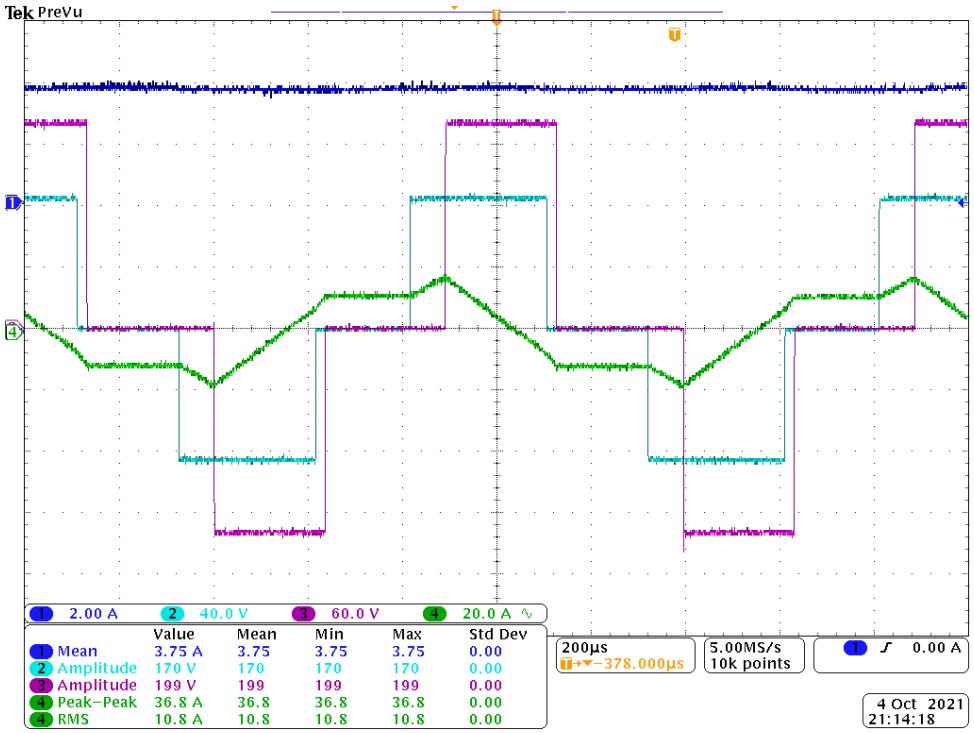


Figure 19. DAB operation under the TPS method at medium power.

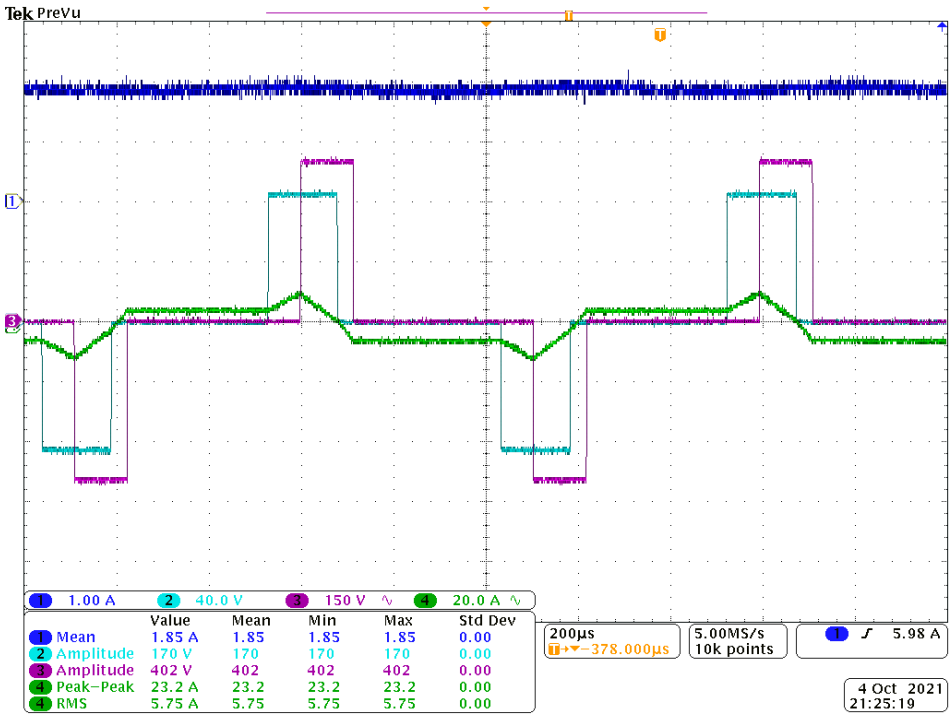


Figure 20. DAB operation under the TPS method at low power.

5.1. Performance of the DAB with RMS Current Minimization

Figures 12–17 show the three operation zones for the DAB converter. Ch1 (blue) is the output DC current, Ch2 (turquoise) is the transformer primary voltage, Ch3 (magenta) is the transformer secondary voltage and Ch4 (green) is the transformer inductor current. The power levels can be identified based on the output DC currents of each of the presented results. The issue of high circulating and peak currents can be seen in the figures demonstrating the SPS method. At the rated power, the peak current reached as high as 68.0 A and the RMS current reached 18.2 A. However, these issues worsen when the converter is operating at reduced power. For half of the rated power, the peak current only decreases by 4.0 A and the RMS current by 0.9 A. At low power, the effect of the high peak and circulating currents is even more severe. From rated power to 25% rated power, the peak current only decreases by 4.8 A and the RMS current by only 0.8 A. These results demonstrate the need for improvement in the control of the DAB converter, especially at a non-rated power operation.

In the DPS method, two equal optimized inner phases, D_1 and D_2, are used in addition to the phase-shift control. At high power operation, the optimized DPS method provided some reduction in the peak current and RMS current compared to the SPS method. However, the effect of the optimized DPS method at reduced power operation is more apparent. At medium power, the peak current is 44.8 A and the RMS current is 14.4 A. At a low power operation, the optimized DPS method reduces the peak current and the RMS current by more than 50%, which significantly improves the performance of the converter at low power.

Figures 18–20 show the performance of the DAB converter using the TPS with the RMS current minimization method under all three operating zones. The TPS control can be seen in the shape of the primary and secondary voltages of the HFT. For the same power levels and voltage rating, it can be seen that the applied TPS control with RMS current minimization strategy provides higher performance compared to both the SPS and DPS methods, as expected. At rated power, the peak and RMS currents are reduced by 9.2 A and 0.5 A, respectively, compared to the SPS method, and 6.8 A and 0.4 A, respectively, compared to the DPS method. At medium power, the peak and RMS currents are reduced further: 27.2 A and 6.5 A, respectively, compared to the SPS method, and 8.0 A and 3.6 A,

respectively, compared to the DPS method. At low power, reductions are also significant in the peak and RMS currents: 40 A and 11.45 A, respectively, compared to the SPS method, and 4.0 A and 3.08 A, respectively, compared to the DPS method. Although improvement is noted at rated power, the greater impact of this technique can be seen at medium and low power operations.

5.2. Performance of the DAB Converter with the Proposed Total PLM Scheme

To further improve the performance of the DAB converter, the proposed total PLM scheme was employed. As noted in the optimization algorithms presented in Table 1, for the high power zone, there is very little room to optimize the performance of the converter. However, at lower power, the optimization method based on the total PLM shows greater superiority than the RMS current minimization scheme. Utilizing total PLM, the three operation zones are presented in Figures 21–23 for the DPS control method. Results for the proposed optimized TPS method with total PLM are shown in Figures 24–26.

It can be seen at high power operation that the optimized TPS method with total PLM provides equal performance to the RMS current minimization method in reducing the peak current and RMS current. However, the effectiveness of the optimized TPS method at reduced power operation is more apparent. At low power operation, the optimized TPS-based PLM method reduces the peak current and the RMS current by 0.8 and 1.04 A, respectively. This significantly improves the performance of the converter at low power. The performance of the SPS, DPS, and TPS modulation techniques for PLM methods are summarized in Table 2.

The total efficiency of the DAB converter was calculated for all power regions for the SPS, DPS, and TPS modulation schemes with the total PLM strategy. Tables 2 and 3 summarize the results. It can be seen that the overall efficiency of the DAB converter was greatly improved by utilizing the TPS method with the total PLM strategy. This was especially true at low power, where the efficiency was 14.51% higher with the TPS method than with the SPS method.

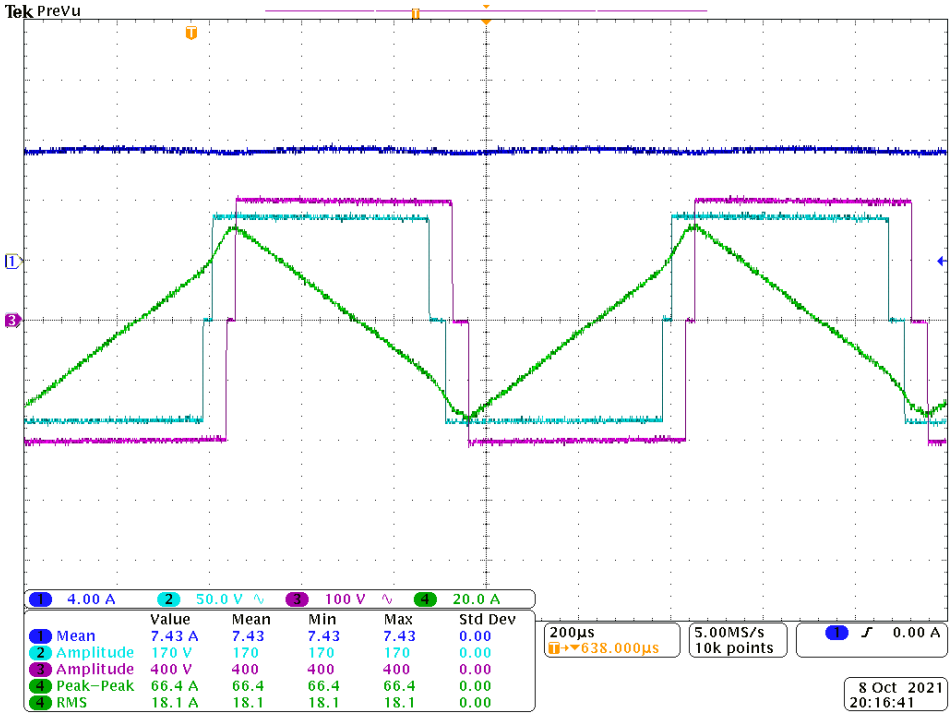


Figure 21. DAB operation at rated power under the DPS-based PLM.

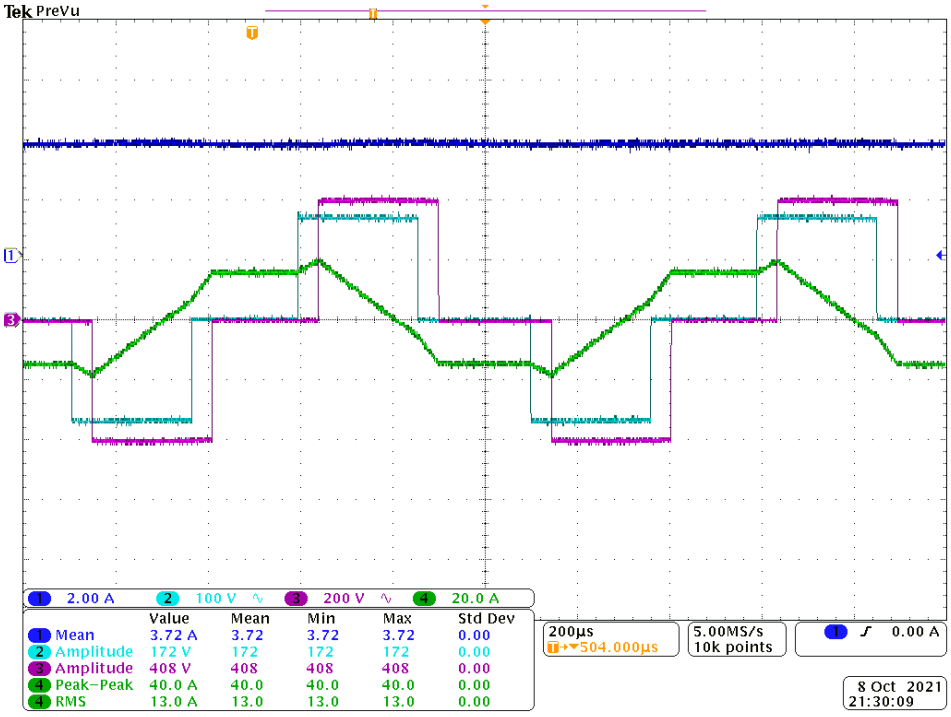


Figure 22. DAB operation at medium power under the DPS-based PLM.

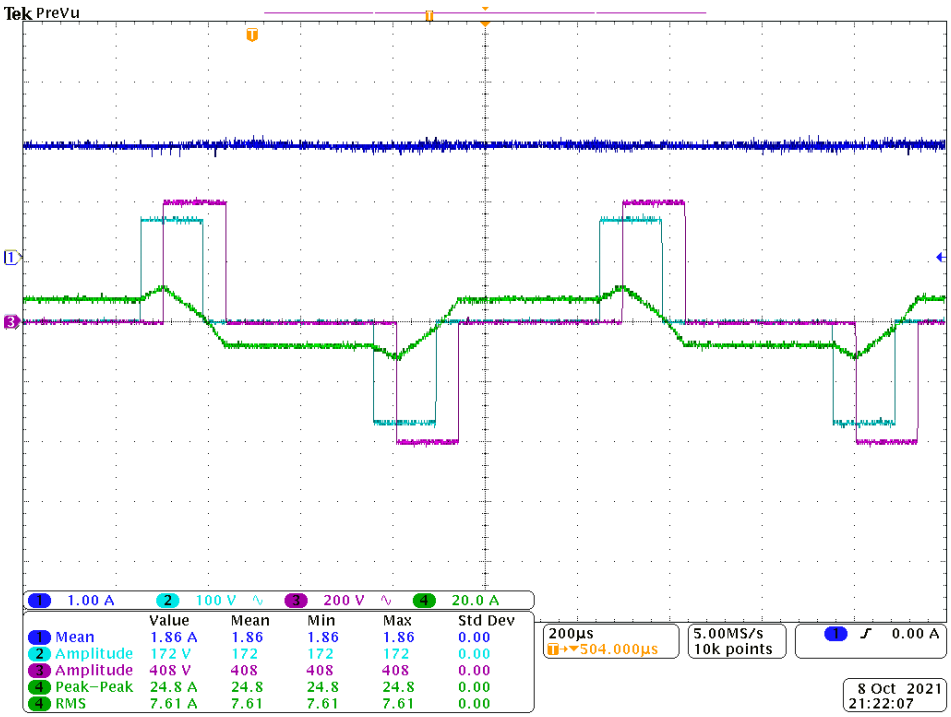


Figure 23. DAB operation at low power under the DPS-based PLM.

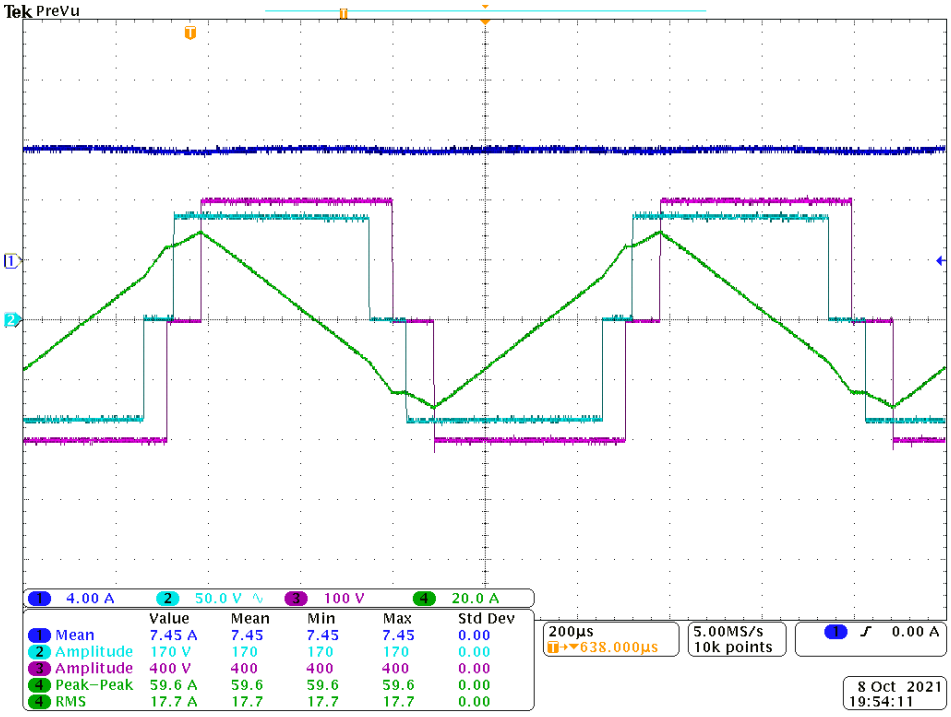


Figure 24. DAB operation at rated power under the TPS-based PLM.

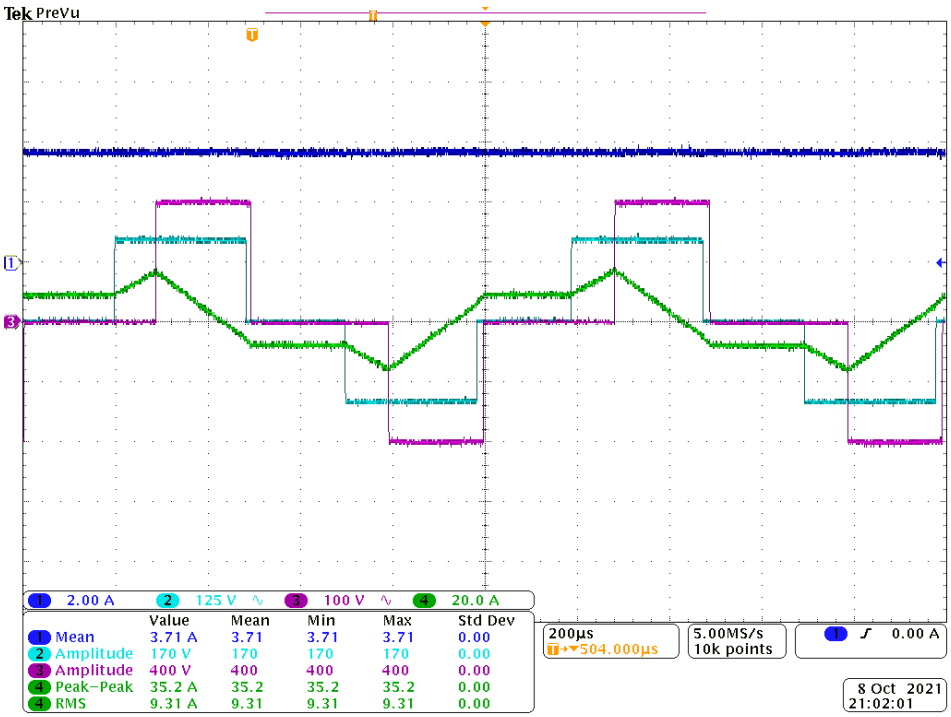


Figure 25. DAB operation at medium power under the TPS-based PLM.

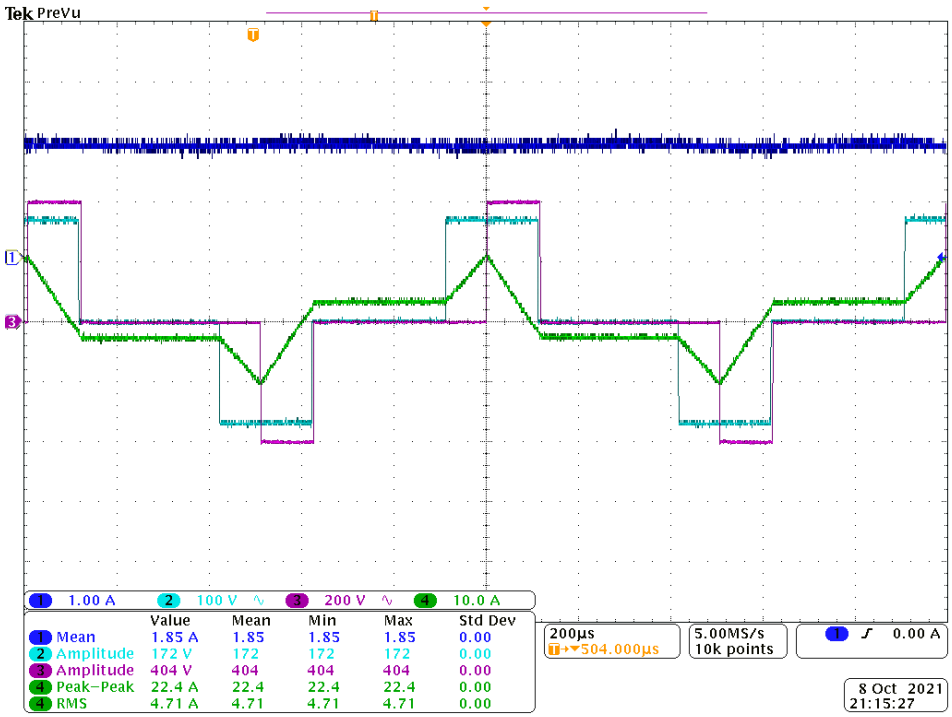


Figure 26. DAB operation at low power under the TPS-based PLM.

Table 2. Performance comparison of the PLM method for rated 1 pu, medium 0.5 pu, and low 0.25 pu power for peak and RMS currents.

$V_1 < V_2$	Zone-3	Zone-2	Zone-1
Objective function	Power Loss	Power Loss	Power Loss
Power Level	1 pu	0.5 pu	0.25 pu
SPS I_{Peak}	68.8 A	64.0A	63.2 A
DPS I_{Peak}	66.4 A	40.0 A	24.8 A
TPS I_{Peak}	59.6 A	35.2 A	22.4 A
SPS I_{RMS}	18.2 A	17.3 A	17.2 A
DPS I_{RMS}	18.1 A	13.0 A	7.61 A
TPS I_{RMS}	17.7 A	9.31 A	4.71 A

Table 3. Performance comparison of the PLM method for rated 1 pu, medium 0.5 pu, and low 0.25 pu power for efficiency.

$V_1 < V_2$	Zone-3	Zone-2	Zone-1
Objective function	Power Loss	Power Loss	Power Loss
Power Level	1 pu	0.5 pu	0.25 pu
SPS efficiency	96.1%	88.56%	77.74%
DPS efficiency	96.58%	92.13%	88.34%
TPS efficiency	98.75%	97.46%	92.25%

6. Conclusions

Although the TPS control method with RMS current minimization can provide some improvement in the efficiency of the system by minimizing conduction and winding losses, the improvement is sub-optimal as the method offers little effect on the switching and core losses. Therefore, in this study, an optimal TPS control strategy with total PLM, which affects all four major sources of loss in the system (conduction, switching, winding, and core losses) was proposed for the DAB converter. The total power loss (covering both

semiconductor and transformer losses) was picked as a cost function to be used in the determination of the control variables for the TPS control method. Detailed formulations of each of the four sources of loss for all three zones of operation were obtained and analyzed for the TPS method. These equations were used to formulate the final total loss expressions for each operation zone. The optimal TPS control variables were then obtained to achieve total PLM based on two optimization methods, PSO and LM. A GO was obtained by using the LM method for the high power level (Zone-3) and, thus, total PLM, RMS current minimization, and peak current minimization were achieved simultaneously. For this operation zone, closed-form expressions were obtained to calculate D_1 and D_2. For Zone-1 and Zone-2, LO was obtained. Therefore, a look-up table was built using the offline PSO technique to determine the control variables for any operating condition. In the case of LO, although the optimal duty cycles that minimized the total power loss were not necessarily the optimal values for the minimum RMS current or peak current stress, they still provided maximum improvement in efficiency due to their inclusion of all four sources of loss. The proposed method was validated with experimental results, and compared with the traditional SPS method, the optimized DPS method, and the TPS method, with the RMS current minimization strategy. The obtained results show the effectiveness of the proposed method, especially for non-rated power conditions.

Author Contributions: Conceptualization, N.A. and A.N.; methodology, N.A. and A.N.; software, G.J.-P., A.E.S.; validation, G.J.-P., N.A. and A.E.S.; formal analysis, A.E.S.; investigation, N.A.; resources, A.N.; data curation, G.J.-P.; writing—original draft preparation, G.J.-P.; writing—review and editing, G.J.-P. and A.N.; visualization, A.E.S.; supervision, N.A. and A.N.; project administration, A.N.; funding acquisition, A.N. All authors have read and agreed to the published version of the manuscript.

Funding: This material is based on work supported by the National Science Foundation under grant no. 1650470. Any opinions, findings, and conclusions or recommendations expressed in this material are those of the author(s) and do not necessarily reflect the views of the National Science Foundation.

Institutional Review Board Statement: Not applicable.

Informed Consent Statement: Not applicable.

Data Availability Statement: Not applicable.

Acknowledgments: Necmi Altin thanks the financial support from the Scientific and Technological Research Council of Turkey (TUBİTAK) BIDEB-2219 Postdoctoral Research Program.

Conflicts of Interest: The authors declare no conflict of interest.

References

1. Doncker, R.W.D.; Divan, D.M.; Kheraluwala, M.H. A threephase soft-switched high power density DC/DC converter for high power applications. *IEEE Trans. Ind. Appl.* **1988**, *1*, 796–805.
2. Shao, S.; Chen, H.; Wu, X.; Zhang, J.; Sheng, K. Circulating Current and ZVS-on of a Dual Active Bridge DC-DC Converter: A Review. *IEEE Access* **2019**, *7*, 50561–50572. [CrossRef]
3. Xue, F.; Yu, R.; Huang, A.Q. A 98.3% efficient gan isolated bidirectional DC–DC converter for DC microgrid energy storage system applications. *IEEE Trans. Ind. Electron.* **2017**, *64*, 9094–9103. [CrossRef]
4. Shiva, S.M.; Gorla, N.B.Y.; Das, P.; Panda, S.K. Tapchanging transformer based dual active bridge bi-directional DC-DC converter. In Proceedings of the 2015 9th International Conference on Power Electronics and ECCE Asia (ICPE-ECCE Asia), Seoul, Korea, 1–5 June 2015; pp. 2025–2030.
5. Chan, Y.P.; Yaqoob, M.; Wong, C.S.; Loo, K.H. Realization of high-efficiency dual-active-bridge converter with reconfigurable multilevel modulation scheme. *IEEE J. Emerg. Sel. Top. Power Electron.* **2020**, *8*, 1178–1192. [CrossRef]
6. Choi, W.; Rho, K.-M.; Cho, B.-H. Fundamental duty modulation of dual-active-bridge converter for wide-range operation. *IEEE Trans. Power Electron.* **2016**, *31*, 4048–4064. [CrossRef]
7. Taylor, A.; Liu, G.; Bai, H.; Brown, A.; Johnson, P.M.; Ammond, M.M. Multiple-phase-shift control for a dual active bridge to secure zero-voltage switching and enhance light-load performance. *IEEE Trans. Power Electron.* **2018**, *33*, 4584–4588. [CrossRef]
8. Karshenas, H.R.; Daneshpajooh, H.; Safaee, A.; Bakhshai, A.; Jain, P. Basic families of medium-power soft-switched isolated bidirectional DC-DC converters. In Proceedings of the 2011 2nd Power Electronics, Drive Systems and Technologies Conference, Tehran, Iran, 16–17 February 2011; pp. 92–97.

9. Guidi, G.; Kawamura, A.; Sasaki, Y.; Imakubo, T. Dual active bridge modulation with complete zero voltage switching taking resonant transitions into account. In Proceedings of the 2011 14th European Conference on Power Electronicsand Applications, Birmingham, UK, 30 August–1 September 2011; pp. 1–10.
10. Inoue, S.; Akagi, H. A bidirectional isolated dc-dc converter as a core circuit of the next-generation medium-voltage power conversion system. *IEEE Trans. Power Electron.* **2007**, *22*, 535–542. [CrossRef]
11. Krismer, F.; Kolar, J.W. Accurate small-signal model for the digital control of an automotive bidirectional dual active bridge. *IEEE Trans. Power Electron.* **2009**, *24*, 2756–2768. [CrossRef]
12. Oggier, G.G.; Garcia, G.O.; Oliva, A.R. Modulation strategy to operate the dual active bridge dc-dc converter under soft switching in the whole operating range. *IEEE Trans. Power Electron.* **2011**, *26*, 1228–1236. [CrossRef]
13. Baiand, H.; Mi, C. Eliminate reactive power and increase system efficiency of isolated bidirectional dual-active-bridge dc–dc converters using novel dual-phase-shift control. *IEEE Trans. Power Electron.* **2008**, *23*, 2905–2914.
14. Hou, N.; Song, W.; Zhu, Y.; Sun, X.; Li, W. Dynamic and static performance optimization of dual active bridge DC-DC converters. *J. Mod. Syst. Clean Energy* **2018**, *6*, 607–618. [CrossRef]
15. Liu, B.; Davari, P.; Blaabjerg, F. An optimized hybrid modulation scheme for reducing conduction losses in dual active bridge converters. *IEEE J. Emerg. Sel. Top. Power Electron.* **2021**, *9*, 921–936. [CrossRef]
16. Noroozi, N.; Emadi, A.; Narimani, M. Performance evaluation of modulation techniques in single-phase dual active bridge converters. *IEEE Open J. Ind. Electron. Soc.* **2021**, *2*, 410–427. [CrossRef]
17. Oggier, G.G.; Garcia, G.O.; Oliva, A.R. Switching control strategy to minimize dual active bridge converter losses. *IEEE Trans. Power Electron.* **2009**, *24*, 1826–1838. [CrossRef]
18. Wen, H.; Xiao, W.; Su, B. Nonactive power loss minimization in a bidirectional isolated DC–DC converter for distributed power systems. *IEEE Trans. Ind. Electron.* **2014**, *61*, 6822–6831. [CrossRef]
19. Zhao, B.; Song, Q.; Liu, W. Efficiency characterization and optimization of isolated bidirectional DC–DC converter based on dual-phase-shift control for DC distribution application. *IEEE Trans. Power Electron.* **2013**, *28*, 1711–1727. [CrossRef]
20. Wu, K.; de Silva, C.W.; Dunford, W.G. Stability analysis of isolated bidirectional dual active full-bridge dc-dc converter with triple phase-shift control. *IEEE Trans. Power Electron.* **2012**, *27*, 2007–2017. [CrossRef]
21. Hou, N.; Song, W.; Wu, M. Minimum-current-stress scheme of dual active bridge DC–DC converter with unified phase-shift control. *IEEE Trans. Power Electron.* **2016**, *31*, 8552–8561. [CrossRef]
22. Huang, J.; Wang, Y.; Li, Z.; Lei, W. Unified triple-phase-shift control to minimize current stress and achieve full soft-switching of isolated bidirectionalDC–DC converter. *IEEE Trans. Ind. Electron.* **2016**, *63*, 4169–4179. [CrossRef]
23. Mou, D.; Luo, Q.; Wang, Z.; Li, J.; Wei, Y.; Shi, H.; Du, X. Optimal asymmetric duty modulation to minimize inductor peak-to-peak current for dualactive bridge DC–DC converter. *IEEE Trans. Power Electron.* **2021**, *36*, 4572–4584. [CrossRef]
24. Hou, N.; Song, W.; Li, Y.; Zhu, Y.; Zhu, Y. A comprehensive optimization control of dual-active-bridge DC–DC converters based on unified-phase-shift and power-balancing scheme. *IEEE Trans. Power Electron.* **2019**, *34*, 826–839. [CrossRef]
25. Sha, D.; Zhang, J.; Liu, K. Leakage inductor current peak optimization for dual-transformer current-fed dual active bridge DC–DC converter with wide inputand output voltage range. *IEEE Trans. Power Electron.* **2020**, *35*, 6012–6024. [CrossRef]
26. Wu, F.; Feng, F.; Gooi, H.B. Cooperative triple-phase-shift controlfor isolated DAB DC–DC converter to improve current characteristics. *IEEE Trans. Ind. Electron.* **2019**, *66*, 7022–7031. [CrossRef]
27. Hebala, O.M.; Aboushady, A.A.; Ahmed, K.H.; Abdelsalam, I. Generic closed-loop controller for power regulation in dual active bridge DC–DC converter with current stress minimization. *IEEE Trans. Ind. Electron.* **2019**, *66*, 4468–4478. [CrossRef]
28. Shao, S.; Jiang, M.; Ye, W.; Li, Y.; Zhang, J.; Sheng, K. Optimal phase-shift control to minimize reactive power for a dual active bridge DC–DCconverter. *IEEE Trans. Power Electron.* **2019**, *34*, 10193–10205. [CrossRef]
29. Das, D.; Basu, K. Optimal design of a dual-active-bridge DC–DC converter. *IEEE Trans. Ind. Electron.* **2021**, *68*, 12034–12045. [CrossRef]
30. Hebala, O.M.; Aboushady, A.A.; Ahmed, K.H.; Abdelsalam, I.; Burgess, S.J. A new active power controller in dual active bridge DC–DC converter with a minimum-current-point-tracking technique. *IEEE J. Emerg. Sel. Top. Power Electron.* **2021**, *9*, 1328–1338. [CrossRef]
31. Zhu, L.; Taylor, A.R.; Liu, G.; Bai, K. A multiple-phase-shiftcontrol for a sic-based EV charger to optimize the light-load efficiency, current stress, and power quality. *IEEE J. Emerg. Sel. Top. Power Electron.* **2018**, *6*, 2262–2272. [CrossRef]
32. Bhattacharjee, A.K.; Batarseh, I. Optimum hybrid modulation for improve-ment of efficiency over wide operating range for triple-phase-shift dual-active-bridgeconverter. *IEEE Trans. Power Electron.* **2020**, *35*, 4804–4818. [CrossRef]
33. Zhou, L.; Gao, Y.; Ma, H.; Krein, P.T. Wide-load range multiobjective efficiency optimization produces closed-form control solutions for dual active bridgeconverter. *IEEE Trans. Power Electron.* **2021**, *36*, 8612–8616. [CrossRef]
34. Pistollato, S.; Zanatta, N.; Caldognetto, T.; Mattavelli, P. A low complexity algorithm for efficiency optimization of dual active bridge converters. *IEEE Open J. Power Electron.* **2021**, *2*, 18–32. [CrossRef]
35. Tong, A.; Hang, L.; Li, G.; Jiang, X.; Gao, S. Modeling andanalysis of a dual-active-bridge-isolated bidirectional DC/DC converter to minimize RMS current with whole operating range. *IEEE Trans. Power Electron.* **2018**, *33*, 5302–5316. [CrossRef]
36. Shen, X.; Ouyang, T.; Chen, Z.; Zhao, S.; Fang, J.; Zhang, Y. Randomized computation for the current stress policy design in the DAB converter. *IEEE Control. Syst. Lett.* **2021**, *5*, 863–868. [CrossRef]

37. Tang, Y.; Hu, W.; Xiao, J.; Chen, Z.; Huang, Q.; Chen, Z.; Blaabjerg, F. Reinforcement learning based efficiency optimization scheme for the DAB DC–DC converter with triple-phase-shift modulation. *IEEE Trans. Ind. Electron.* **2021**, *68*, 7350–7361. [CrossRef]
38. Tang, Y.; Hu, W.; Cao, D.; Hou, N.; Li, Y.; Chen, Z.; Blaab-jerg, F. Artificial intelligence-aided minimum reactive power control for the DAB con-verter based on harmonic analysis method. *IEEE Trans. Power Electron.* **2021**, *36*, 9704–9710. [CrossRef]
39. Jean-Pierre, G.; Khayamy, M.; Altin, N.; Shafei, A.E.; Nasiri, A. A Triple Phase-Shift Based Control Method for RMS Current Minimization and Power Sharing Control of Input-Series Output-Parallel Dual Active Bridge Converter. In Proceedings of the 2020 IEEE Transportation Electrification Conference & Expo (ITEC), Chicago, IL, USA, 23–26 June 2020; pp. 550–555. [CrossRef]
40. Venkatachalam, K.; Sullivan, C.; Abdallah, T.; Tacca, H. Accurate prediction of ferrite core loss with nonsinusoidal waveforms using only Steinmetz parameters. In Proceedings of the IEEE Workshop on Computers in Power Electronics, Mayaguez, PR, USA, 3–4 June 2002; pp. 36–41.
41. Jean-Pierre, G.; Altin, N.; Shafei, A.E.; Nasiri, A. Efficiency Optimization of Dual Active Bridge DC–DC Converter with Triple Phase-Shift Control. In Proceedings of the 2020 IEEE Energy Conversion Congress and Exposition (ECCE), Detroit, MI, USA, 11–15 October 2020; pp. 1217–1222. [CrossRef]
42. Kennedy, J.; Eberhart, R. Particle swarm optimization. In Proceedings of the ICNN'95-International Conference on Neural Networks, Perth, Australia, 27 November–1 December 1995; Volume 4, pp. 1942–1948.